ARTICLES
https://doi.org/10.1038/s41594-020-0508-3

nature structural & molecular biology

The condensin holocomplex cycles dynamically between open and collapsed states

Je-Kyung Ryu[1], Allard J. Katan[1], Eli O. van der Sluis[1], Thomas Wisse[1], Ralph de Groot[1], Christian H. Haering[2] and Cees Dekker[1]✉

Structural maintenance of chromosome (SMC) protein complexes are the key organizers of the spatiotemporal structure of chromosomes. The condensin SMC complex has recently been shown to be a molecular motor that extrudes large loops of DNA, but the mechanism of this unique motor remains elusive. Using atomic force microscopy, we show that budding yeast condensin exhibits mainly open 'O' shapes and collapsed 'B' shapes, and it cycles dynamically between these two states over time, with ATP binding inducing the O to B transition. Condensin binds DNA via its globular domain and also via the hinge domain. We observe a single condensin complex at the stem of extruded DNA loops, where the neck size of the DNA loop correlates with the width of the condensin complex. The results are indicative of a type of scrunching model in which condensin extrudes DNA by a cyclic switching of its conformation between O and B shapes.

The SMC family of protein complexes, which includes condensin, cohesin and the SMC5–SMC6 complex, has vital roles in spatially organizing chromosomes, as its members are key in sister-chromatid cohesion; chromosome condensation, segregation and resolution; and DNA replication and DNA-damage repair[1–5]. Structurally, SMC protein complexes feature a circularly connected conformation of a kleisin–SMC heterodimer ring (Fig. 1a).

Hi-C studies and polymer simulations have suggested that mitotic chromosomes consist of long DNA loops extruded by condensin complexes[6–12]. The formation of these loops requires a processive motor that extrudes DNA. Recent single-molecule fluorescence studies have indeed demonstrated a motor function[13] and have provided direct evidence for DNA-loop extrusion by the yeast condensin complex[14]. Condensin constitutes a unique new type of DNA-translocase motor that reels in DNA at high speeds (up to 1.5 kbp s^{-1} at low forces) while consuming low ATP, that is at an ATPase rate of ~2 ATP s^{-1}, implying that the motor takes very large steps (~50 nm) per ATP molecule that is hydrolyzed[14]. While this large step size suggests that the motor action involves sizeable conformational changes at the level of the size of the full SMC complex, it is currently unclear by which molecular mechanism condensin is able to process DNA so efficiently.

Studying the conformational changes of condensin and its connection to ATP hydrolysis for structural changes of the protein complex is thus critical to understanding the mechanism underlying DNA-loop extrusion by condensin. Many studies have been undertaken to resolve the structure of a variety of SMC proteins, with contradictory results so far[15]. Negative-staining electron microscopy (EM) structures and cross-linking experiments have suggested a rigid extended structure (I shape) of prokaryotic SMCs, whereas ATP-dependence studies have indicated a transition from I to O shapes upon ATP hydrolysis[16–18]. Recent EM studies on MukBEF and yeast cohesin have suggested that there are transitions between an extended and a folded state[19,20], similar to an early AFM study on *Schizosaccharomyces pombe* condensin[21]. High-speed (HS) AFM images of yeast condensin SMC dimers only in liquid showed instead very flexible SMC arms and dynamical conformational changes between O, V, P and B shapes[22]. However, thus far, no HS liquid AFM studies on the full condensin holocomplex with all its subunits have been reported.

Here, we resolve the conformational states and shape transitions of yeast condensin and its binding configuration to DNA, with the aim to understand the motor dynamics that drive DNA-loop extrusion. AFM imaging comes with particular advantages: it features a high resolution (*xy* resolution, ~1 nm; *z*, resolution, ~0.1 nm), it provides high contrast and it is free of labels and cross-links, making it excellent for studying complex DNA-protein interactions. Dry AFM imaging, wherein the sample is dried after the molecules are incubated on a surface, enables high-throughput imaging by capturing many molecules in various conformations, including intermediates of loop extrusion. HS AFM in liquid even enables imaging of real-time structural changes of condensin within a physiological buffer in the presence of ATP, with a temporal resolution up to 20 frames s^{-1}, although it features a lower throughput owing to the small imaging area (~100 × 100 nm^2) that is needed to realize a high frame rate[23–25].

A major finding from our study is that the condensin holocomplex predominantly exhibits either an open O shape or a collapsed B shape, and that it cycles back and forth between these states in an ATP-dependent fashion. In addition, we find that the SMC arms are highly flexible and that condensin binds to DNA both at its hinge and at its globular domains (that is, the HEAT (Huntingin, EF3, PP2A, TOR1)-repeat subunits and SMC ATPase head domains). These findings suggest that there is a motor mechanism through which toggling between O and B shapes of condensin periodically transfers DNA between two different DNA-binding sites, one near the hinge and one near the globular domain—consistent with some form of a scrunching model.

Results

Condensin exhibits open O or collapsed B shapes. Figure 1b shows an example of an AFM image of individual *Saccharomyces cerevisiae* condensin holocomplexes in the absence of ATP. The purified complexes showed DNA-stimulated ATPase activity and

[1]Department of Bionanoscience, Kavli Institute of Nanoscience Delft, Delft University of Technology, Delft, the Netherlands. [2]Cell Biology and Biophysics Unit, Structural and Computational Unit, European Molecular Biology Laboratory (EMBL), Heidelberg, Germany. ✉e-mail: c.dekker@tudelft.nl

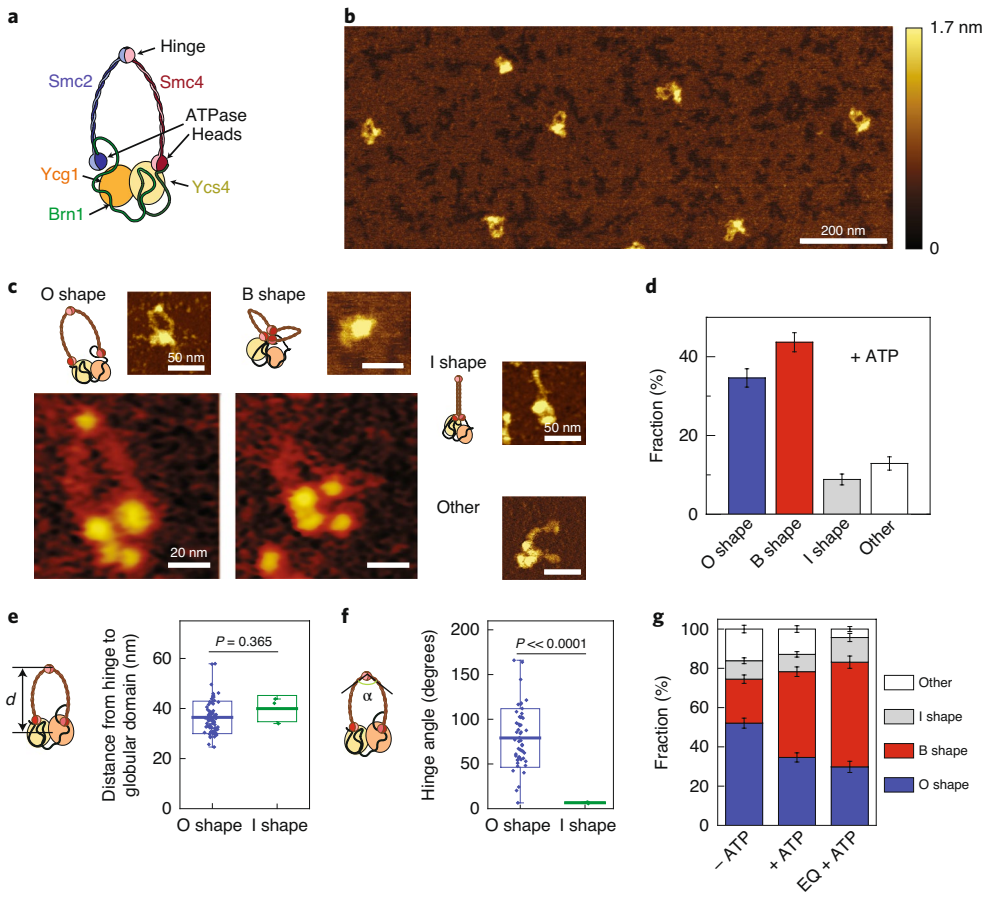

Fig. 1 | The condensin holocomplex exhibits different shapes. a, Cartoon model of the yeast condensin holocomplex. Two coiled-coil arms folded antiparallel, Smc2 and Smc4 (each ~45 nm in length), link an interconnected hinge domain at one end to an ATP-binding cassette (ABC)-type nucleotide-binding head domain at the other end, whereas the two head domains are connected by the Brn1 kleisin subunit. Two HEAT-repeat subunits, Ycs4 and Ycg1, are bound to the kleisin. **b**, Representative dry-AFM image of condensin holocomplexes in the absence of ATP ($n = 7$ independent experiments from 7 independently purified proteins). **c**, Representative images of various conformations of condensin holocomplexes. Small panels are dry-AFM images ($n = 7$ independent experiments) and large panels are liquid-AFM images ($n = 6$ molecules, 3 independent experiments from 2 independently purified proteins) of the O, B and I shape. **d**, Relative occurrence of different states in the presence of ATP (mean ± s.d.; $n = 419$ individual complexes from dry-AFM images). **e**, Distance between hinge and the globular domain for O-shaped and I-shaped condensins. **f**, Hinge angle measured at the hinge domain. *P* values were assessed by the two-tailed Student's *t*-test (**e**,**f**). The box plots span from mean − s.d. to mean + s.d., the center thick lines show the mean and the whiskers represent minimum and maximum values (**e**,**f**). **g**, Relative occurrence of various conformations ($n = 384$, 419 and 255 individual complexes without ATP, individual complexes with ATP and the EQ mutant with ATP, respectively). Error bars are counting errors in **d** and **g**.

extruded DNA loops (Extended Data Fig. 1), similar to earlier reports[14]. The AFM images showed a homogeneous volume distribution (Fig. 1b and Extended Data Fig. 2a). We were able to resolve the SMC arms in most of our condensin images, as well as to distinguish various conformational states of the condensin holocomplexes[22] (Fig. 1c–g).

The main configurations that condensin adopted were O and B shapes (Fig. 1c). O-shaped complexes exhibited a ring-like configuration with two long arms, a large globular domain at one end and a smaller domain at the other end. The latter likely corresponds to the Smc2–Smc4 hinge dimerization domain, whereas the large globular domain is presumably composed of the Smc2–Smc4 ATPase heads, the Brn1 kleisin subunit and the two HEAT-repeat subunits Ycs4 and Ycg1. Whereas these subunits could not be resolved in dry AFM, liquid-phase AFM frequently allowed for resolution of individual subunits within the large globular domain (Fig. 1c). Over time, the SMC arms displayed a very dynamic behavior, adopting many different configurations, which shows that they are structurally flexible. The average distance between the center of mass of the globular and hinge domains in the O-shaped conformation was 37 ± 7 nm (mean ± s.d.) (Fig. 1e), with an opening angle between the coiled coils at the hinge domain of 102 ± 51° (mean ± s.d.) (Fig. 1f). In the presence of ATP, the most prominent state that we observed for condensin holocomplexes was a collapsed B-shaped conformation. This state presumably corresponds to the 'butterfly shape' previously described for SMC-dimer-only samples[22], which is formed when the hinge domain engages the joined SMC-head domains.

The data in Fig. 1 represent molecules deposited onto untreated mica, which carries a negative charge. To rule out surface-charge effects on the conformation of the proteins, we also imaged condensin holocomplexes on positively charged polylysine-treated mica. This yielded the same result (Extended Data Fig. 2c), indicating that these conformations were not induced by electrostatic surface-protein interactions. Together, the O and B shapes accounted for the vast majority (78%) of all observed conformations. In addition, we observed smaller fractions of I shapes (9%) and other shapes (13%, Extended Data Fig. 2d). In I-shaped molecules, the two SMC arms were presumably coaligned, and the distance between hinge and globular domains was slightly larger than that in the O-shaped conformation, as expected (Fig. 1e).

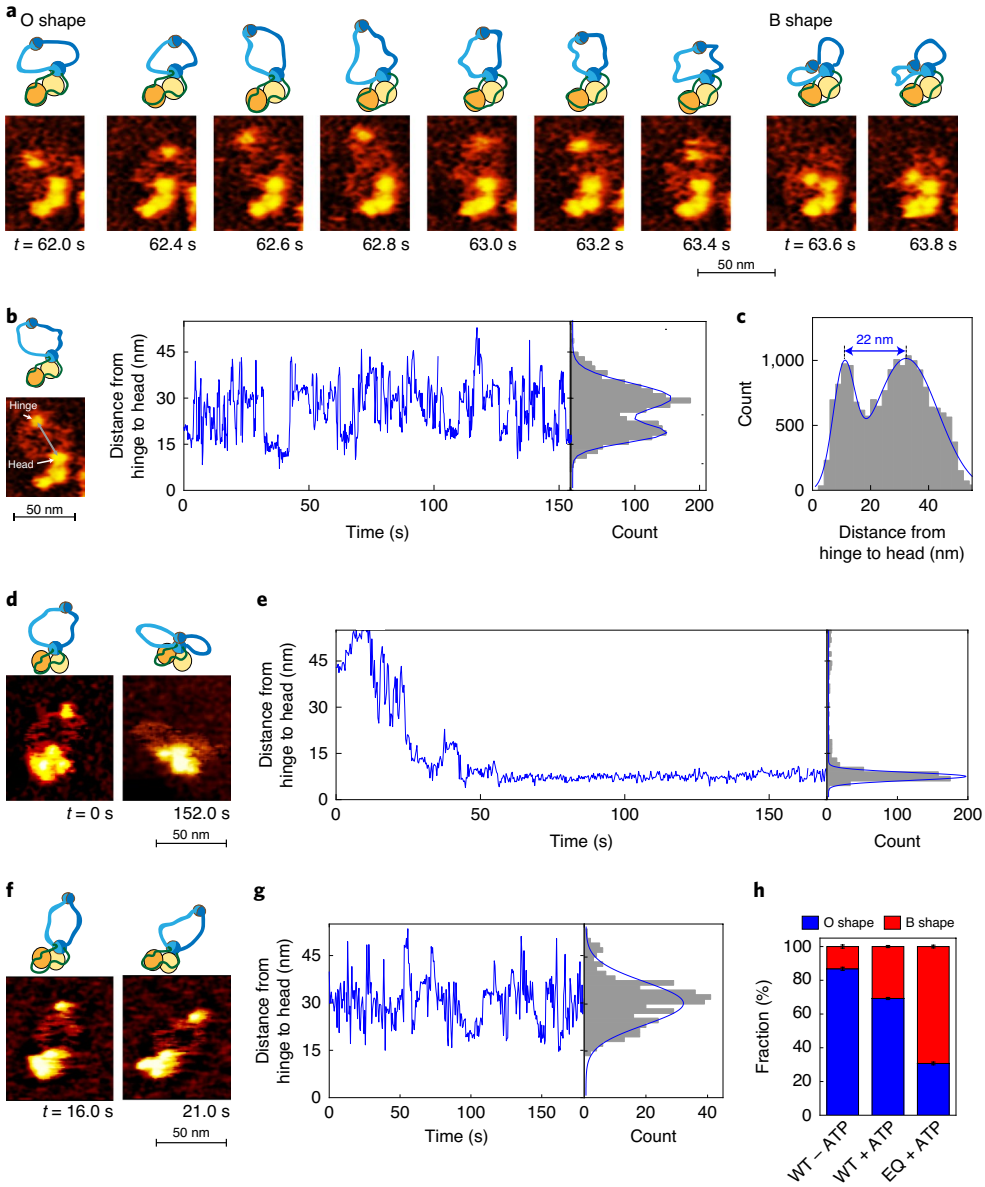

Fig. 2 | Condensin dynamically toggles between an O shape and a B shape over time. a, Representative HS liquid-AFM images of the wild-type condensin holocomplex in the presence of ATP followed over time at a 5 frames s^{-1} rate (Supplementary Video 1) ($n = 6$ molecules, 3 independent experiments, 2 independent protein purifications). The complex changes its conformation over time from an O shape (62–63.5 s) to a collapsed B shape (after 63.5–64 s). **b**, Real-time trace of the hinge–head distance. The distance is seen to toggle between a large and small value, corresponding to the O and B shapes, respectively. The distribution of the distance from hinge to head, depicted on the right, shows two peaks. The solid line is a fit of two Gaussians. **c**, Distributions of the distance from hinge to head ($n = 8{,}712$ frames from 26 SMC molecules). The peak-to-peak distance is 22 ± 13 nm (mean ± s.d.). **d**, Representative HS liquid-AFM images of the EQ mutant condensin holocomplex with ATP ($n = 2$ independent experiments). **e**, Representative real-time trace of the distance from hinge to head for the EQ mutant plus ATP and the distribution of the distance from hinge to head (right) showing a single peak at a short distance (7.5 ± 1.3 nm, mean ± s.d.) ($n = 8$ SMC molecules). **f**. Representative HS AFM images of wild-type condensin without ATP ($n = 3$ independent experiments). **g**, Representative real-time trace of distance from hinge to head and the distribution of the distances (right). These data show a dynamic O-shaped condensin with a large distance (30 ± 7 nm, mean ± s.d.) ($n = 6$ SMC molecules). **h**, Relative occurrence of B shapes and O shapes. $n = 1{,}309$ frames (6 molecules) for wild-type without ATP, $n = 5{,}240$ frames (12 molecules) for wild-type with ATP and $n = 3{,}239$ frames (8 molecules) for EQ mutant plus ATP. Data shown as mean ± s.d. Error bars are counting errors.

Different ATP states yielded different distributions of O and B shapes. We performed AFM experiments under several conditions: with ATP, without ATP and using an 'EQ' mutant version with single amino-acid substitutions in the Walker B motifs of the Smc2 and Smc4 active sites ($Smc2_{E1113Q}$–$Smc4_{E1352Q}$), which allow ATP binding but drastically reduce nucleotide hydrolysis. In the presence of ATP, we observed slightly more B shapes than O shapes, and this fraction increased further with the EQ mutant complex (Fig. 1g). In contrast, we found significantly more open O states than collapsed B states in the absence of ATP. These numbers suggest that the collapsed B state might be promoted by ATP binding to the head domains and that hydrolysis and release of ATP are associated with a release of the hinge domain from the head domains into the open O shape.

Condensin cycles back and forth between an open O shape and a collapsed B shape. We applied HS AFM imaging to visualize the

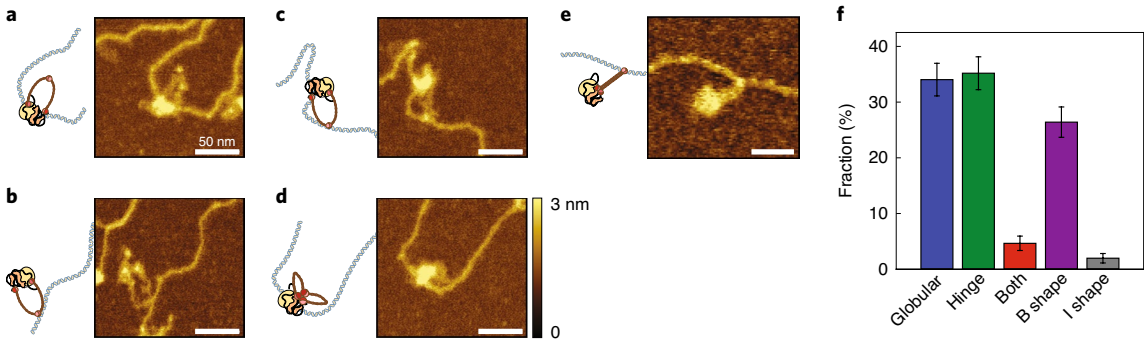

Fig. 3 | Binding of condensin to DNA in the presence of ATP. a, Binding of condensin to DNA through its globular domain ($n = 88$ molecules). **b**, Binding of condensin to DNA through its hinge domain ($n = 89$ molecules). **c**, Binding of condensin to DNA at both hinge and globular domains ($n = 69$ molecules). **d**, Collapsed B-shape condensin on DNA ($n = 11$ molecules). **e**, I-shape condensin on DNA ($n = 5$ molecules). **f**, Relative occurrence of each of the binding modes ($n = 5$ independent experiments and $n = 262$ molecules). Data shown as mean ± s.d. Error bars are counting errors.

dynamics of the conformational changes of condensin holocomplexes in a buffer that contained 50 mM NaCl and 1–2 mM ATP—equivalent to the buffer in which condensin exhibits DNA-loop extrusion in vitro (Extended Data Fig. 1c)[14]. From movies recorded at 5 frames s^{-1} (Fig. 2 and Supplementary Videos 1–4), we were able to resolve 3 or 4 substructures within the globular domain; see, for example, Fig. 2a and Extended Data Fig. 3, in which, in addition to the SMC arms and hinge domain, the dimerized head domains and 2 HEAT-repeat subunits are distinguishable. The SMC arms in the condensin holocomplex were very dynamic and flexible, changing conformations very fast (that is, <0.2 s; Fig. 2a), very similar to previous studies on SMC-dimer-only samples[22]. For the O shapes, we also observed that the mutual angle between the two SMC arms at the hinge changed dynamically (Extended Data Fig. 4a–c).

Interestingly, we observed clear dynamic conformational changes wherein condensin would toggle between an O shape and a collapsed B shape, and vice versa (Fig. 2a, b, Extended Data Fig. 3 and Supplementary Videos 1–4). In these movies, the hinge region transitioned between a far-away position and a location close to the globular domain, consistent with an overall shape change between the O and B shapes, respectively (Fig. 2a,b). Quantification of this dynamic behavior is provided in Fig. 2c, which plots the distance from hinge to head as measured between their centers of masses (compare with inset, Fig. 2b). The data clearly exhibit a two-level-fluctuator behavior, displaying two distinct peaks in the histogram (Fig. 2b, right). The distance between these peaks, averaged over multiple such traces ($n = 26$), is 22 ± 13 nm (mean ± s.d.) (Fig. 2c). The transition between the O-shape and the B-shape state could be completed very fast, faster than the temporal resolution of our imaging method (0.2 s). Note that the hinge movement was not strongly affected by tip-sample interactions, because the hinge movement was isotropic and not biased by the AFM scanning direction (Extended Data Fig. 5).

It is noteworthy that we did not observe I shapes during the conformational changes. For a quantitative analysis, we measured the mutual distance between the midpoints of the two SMC arms within a holocomplex (Extended Data Fig. 4d). We never observed the two SMC arms to be in close proximity, but measured a mutual distance that was much larger than the width of an individual SMC arm (Extended Data Fig. 4e,f). In addition, the opening angle between the coiled-coil arms measured at the hinge was consistently large, in agreement with open conformation (Extended Data Fig. 4a–c).

To investigate how ATP binding influences the switching of the conformations between O and B shapes, we performed HS AFM imaging for the EQ mutant condensin holocomplex in the presence of ATP (ATP-bound state) and for the wild-type condensin holocomplex without ATP (apo state). For the EQ mutant with ATP, we mostly observed stable B shapes. We also managed to record the transition from O to B shapes for the EQ mutant in the presence of ATP (Fig. 2d,e and Supplementary Video 5). Wild-type condensin without ATP remained in the O shape most of the time, exhibiting dynamic hinge movements without the hinge approaching the globular domain (Fig. 2f,g and Supplementary Video 6). These HS AFM results thus provide strong evidence that ATP binding is associated with a conformation in which condensin is collapsed into a B shape. The finding that the hinge can fold back onto the globular domain is consistent with a recent cryo-EM study of cohesin in the ATP-bound state, in which the hinge region contacts the SA1 HEAT-repeat subunit[26]. In contrast to the large changes in the distance between hinge and head (Fig. 2c), we observed a constant mutual distance between the two HEAT-repeat subunits in the presence of ATP in liquid AFM movies where we could resolve them (Extended Data Fig. 4g–i).

Condensin binds double-stranded DNA via its globular and hinge domains. In order to reel in DNA during loop extrusion, the condensin motor complex must exhibit multiple DNA-binding sites. We used dry AFM to examine the binding of condensin to DNA in the presence of ATP. The images showed different binding modes (Fig. 3). First, as expected, we observed condensin complexes that bound DNA at their globular domain (Fig. 3a), possibly at the Ycg1–Brn1 interface[27]. Second, we observed binding of condensin to DNA via the hinge domain (Fig. 3b). Unexpectedly, the fraction of condensin holocomplexes that contacted DNA via their hinge domain was similar to the fraction of complexes that bound DNA via their globular domain (Fig. 3f). Third, we observed condensin complexes in which both hinge and globular domains were simultaneously in contact with DNA (Fig. 3c). We also observed condensin complexes on DNA that were in the collapsed B shape (Fig. 3d). We rarely observed I shapes on DNA (2%; Fig. 3e), suggesting that the I shape is not a major conformational class of condensin complexes that are bound to DNA. For DNA-bound EQ mutant condensin complexes in the presence of ATP, we observed more collapsed B shapes and fewer O shapes also on DNA (Extended Data Fig. 6a), consistent with the notion that ATP binding induces a change from the O to the B shape (Extended Data Fig. 6b).

A number of control experiments support these conclusions. First, we established that an accidental colocalization, that is a possible fortuitous overlap of DNA and unbound condensin, can account for only a minor fraction of the condensin complexes observed on DNA in the presence of ATP (Extended Data Fig. 7). Second, the fraction of wild-type complexes that contacted DNA was significantly higher than the fraction of mutant complexes that lacked the Ycg1 HEAT-repeat subunit (Extended Data Fig. 7b), consistent with

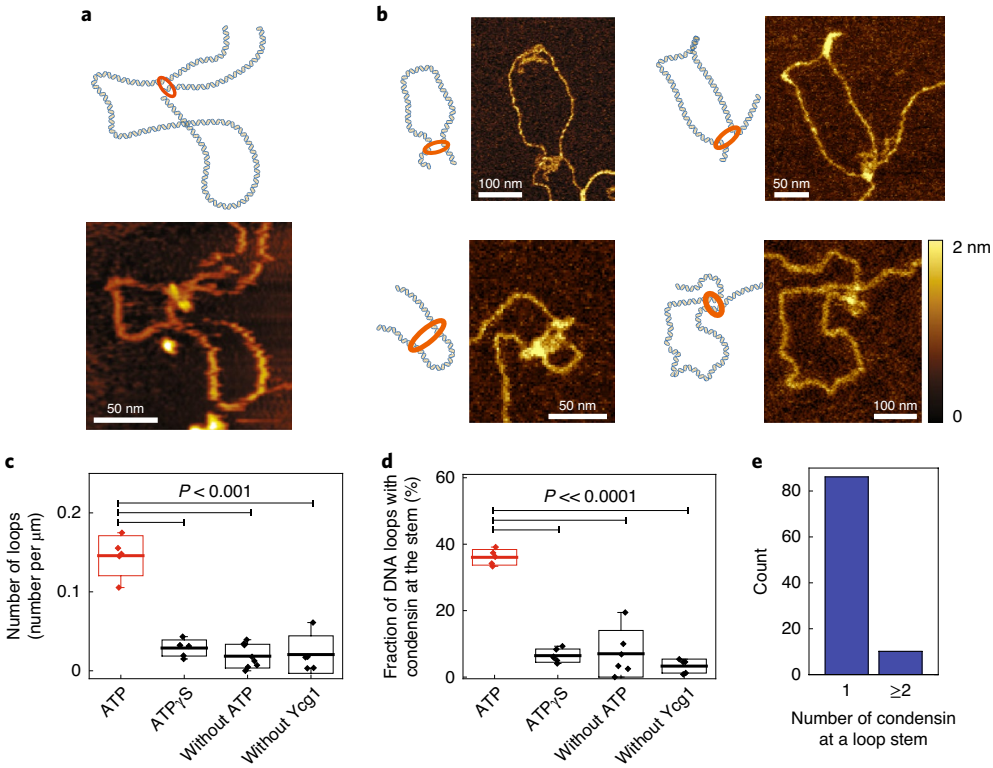

Fig. 4 | DNA loops extruded by condensin. a,**b**, Representative condensin-mediated DNA loops imaged using liquid AFM (in **a**) and dry AFM (in **b**) ($n = 9$ independent experiments). Cartoons are schematics of the images of condensin at the stem of the DNA loops. **c**, Number of DNA loops per µm of DNA under various conditions: with ATP ($n = 5$ independent experiments and 150 loops), with ATPγS ($n = 6$ independent experiments and 21 loops), without ATP ($n = 8$ independent experiments and 24 loops) and without Ycg1 ($n = 5$ independent experiments and 15 loops). **d**, Fraction of DNA loops with condensin localized at the stem of the DNA loop, with various controls ($n = 5$, 6, 8 and 5 independent experiments). The box plots span from mean − s.d. to mean + s.d., the center thick lines show the mean and the whiskers represent minimum and maximum values (**c**,**d**). **e**, Distribution of the number of condensin complexes found at the stem of a DNA loop ($n = 96$). In **c** and **d**, errors are s.d., and *P* values shown were obtained using two-tailed Student's *t*-test.

a previous study that showed that Ycg1 in the globular domain is important for DNA binding[28]. Third, we observed a decrease in the number of condensin complexes that did bind DNA when we omitted ATP, consistent with previous observations that ATP hydrolysis is needed to topologically load condensin onto DNA and increase condensin's residence time on DNA[14].

DNA loops feature a single condensin complex at their stem. We next focused on condensin holocomplexes at the stem of loops of DNA. Both in liquid and dry AFM, we observed a clear colocalization of condensin and the stems of DNA loops (Fig. 4a,b and Supplementary Video 7). We conclude that these loops were predominantly formed by condensin in an ATP-hydrolysis-dependent manner, on the basis of the following observations. First, the percentage of colocalization of condensin and DNA loops was much higher than could be expected from random colocalization (Methods and Extended Data Fig. 8c–e). Second, DNA-loop sizes were significantly larger when DNA had been incubated with wild-type condensin and ATP, compared with when it had been incubated with any negative control (Extended Data Fig. 8a,b); similarly, the number of loops depended strongly on the availability of hydrolyzable ATP (Fig. 4c,d). Negative controls without nucleotide or with the non-hydrolyzable ATP analog ATPγS showed a significantly lower number of loops per unit DNA length (Fig. 4c). Finally, we rarely observed loops when using a tetrameric *S. cerevisiae* condensin complex that lacks Ycg1 (Fig. 4c). Taken together, these experiments strongly indicate that condensin localized to the stem of the DNA loops that it had extruded.

We quantified the number of condensin molecules at the stem of the DNA loops by estimating their volume. We found that 90% of the DNA loops showed a single condensin at the loop stem (Fig. 4e), consistent with an earlier estimate from optical measurements[14] and confirming that a single condensin holocomplex is responsible for the extrusion of a DNA loop. We rarely observed multimeric forms of condensin at the stems of the DNA loops in our experimental conditions. Our observation of a single condensin complex at the DNA-loop stem contrasts with suggestions of the handcuff model, in which loop extrusion by cohesin was suggested to be driven by dimeric SMC complexes[29].

The neck width of the DNA-loop stem correlates to the size of the condensin complex. We then examined the correlation between the neck width at the stem of the DNA loop and the width of the condensin molecule located there (Fig. 5 and Methods). We found a clear linear relationship between the width of the DNA loop at the stem and the characteristic size of the protein at the neck (correlation coefficient $r^2 = 0.87$; Fig. 5b and Extended Data Fig. 9c) for the largest fraction of molecules. This strong tendency suggests that the width of the DNA neck is determined by the size of the condensin holocomplex. A smaller fraction of molecules (blue data in Fig. 5b and Extended Data Fig. 9d) showed no correlation between the DNA-neck width and condensin size. Individual images of these molecules imply that they are the consequence of interwinding DNA upon depositing the DNA onto the polylysine-treated mica surface (Extended Data Fig. 9), which has been extensively characterized previously[30], an effect that we minimized by using a very low

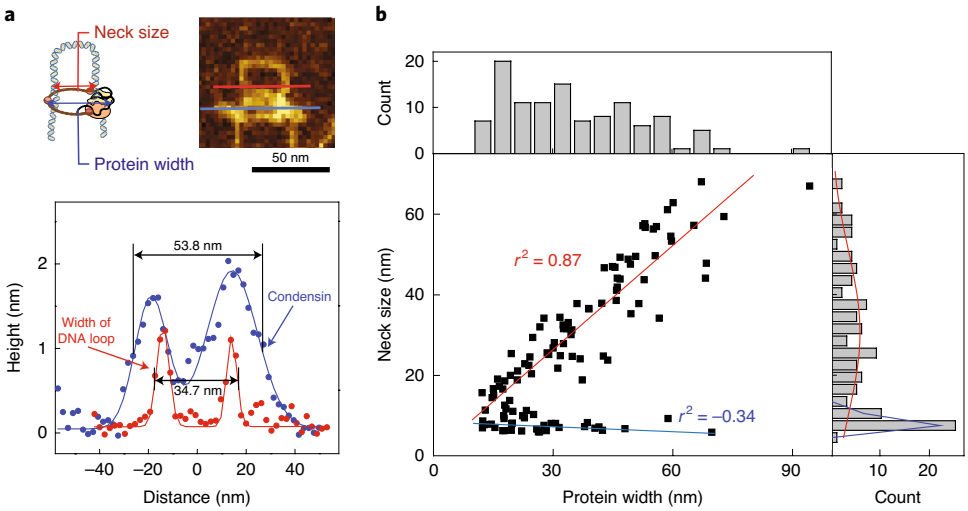

Fig. 5 | The neck size of the DNA loop correlates with the size of the condensin complex. a, Top left schematic indicates the protein width and size of the DNA-loop neck. Lines in the image on the top right indicate where cross-sectional height profiles were acquired, with the result denoted at the bottom panel. For comparison, both the DNA-neck width and protein width were defined as the distances between the two outer points of the full-width half maximums of the Gaussian fits, because separated peaks could not always be resolved when the two DNA segments were too close. **b**, Neck size of DNA loops versus width of condensin at the loop stem. Every point corresponds to a measurement of a single loop ($n = 3$ independent experiments, and 115 molecules). The distribution of neck sizes (shown on the right) is fitted to two Gaussians, yielding average peak values of 9 ± 1 and 31 ± 20 nm (mean ± s.d.).

concentration of polylysine (0.00001%). Overall, our data suggest that conformational changes of the condensin complex are associated with changes in the width of the stem of the DNA loop that had been extruded by condensin.

Discussion

In summary, we visualized yeast condensin holocomplexes on their own as well as bound to DNA. We found that condensin predominantly exhibits an open O shape or a collapsed B shape, and that it dynamically switches between these conformations. When we added condensin to DNA, it bound DNA at the hinge or at the globular domain that is formed by the SMC heads, the kleisin subunit and the HEAT-repeat subunits. We observed a single condensin located at the stem of a DNA loop, where the loop-stem width correlated with the condensin size. Below, we discuss the relevance and importance of these findings.

Flexible SMC arms. Our HS liquid AFM imaging showed very flexible SMC arms with highly dynamic conformational changes. This is very similar to previous observations for the coiled-coil arms of only the Smc2–Smc4 dimers, which exhibited a persistence length of only 4 nm (ref. [22]). The flexibility of SMC arms is therefore not influenced by the interaction with the non-SMC subunits and is a general feature of yeast condensin, and presumably of other SMC holocomplexes. While the HS AFM images unambiguously showed flexible SMC arms, techniques such as X-ray crystallography, cross-linking experiments and EM[16,18] have reported more rigid SMC arms. For Rad50, a related SMC-like protein, liquid-phase imaging similarly revealed flexible and dynamical coiled-coil arms[31,32], and crystal structures implied that the rods were rigid[33]. HS AFM provides a liquid-phase imaging technique that can visualize dynamic changes of the SMC complexes with high spatial and temporal resolution, which could be missed in more-conventional structural techniques.

Conformation of the condensin complex. Our data show that condensin predominantly exhibits an extended O shape or collapsed B shape, depending on its ATP state. This fits observations in an early AFM study and a recent EM paper that showed both extended and compacted configurations of condensin[21] and other SMC proteins[19]. However, our data showed only a small minority fraction of the juxtaposed I shape that was reported in these and other studies[16,18]. The discrepancy of O versus I shape observations among various studies may result from different techniques and sample-preparation methods that can induce or bias the observation of certain configurations. Cryogenic EM (Cryo-EM) has superb resolution in imaging uniform static structures, but also can face challenges with selection bias[34], preferred orientations[35] denaturation of proteins[36] due to the air–water interface. AFM is uniquely able to resolve dynamic structures at the molecular scale, albeit for molecules bound to a surface and at lower resolution than is achievable with cryo-EM.

Occasionally, with a fortuitously good AFM tip in our liquid AFM, we could distinguish various subunits within the globular domain of the condensin holocomplex that is formed by the Smc2 and Smc4 ATPase head domains, the Brn1 kleisin subunit and the two HEAT-repeat subunits Ycg1 and Ycs4. Unfortunately, we could not consistently resolve individual subunits in all data, and hence we refrain from assigning subunit names to individual constituents within the globular domain. We could, however, reliably resolve the basic structure of the SMC holocomplex (that is, the SMC hinge, arms, globular domain) in all analyzed data and could clearly determine the mutual motion between the hinge and globular domain in HS AFM movies (Supplementary Videos 1–4). For determining the mutual distance between Ycg1 and Ycs4 (Extended Data Fig. 4a–c), we used a subset of data in which these units were clearly distinguishable from the SMC heads.

A key observation from the current work is that condensin dynamically cycles between an open O shape and a collapsed B shape over time. Our data for the EQ mutant condensin showed collapsed B shapes, allowing identification of ATP binding inducing the O-to-B transition as a critical step in the mechanochemical cycle.

DNA-binding sites of the condensin complex. Our AFM images of DNA-bound condensin show that condensin can bind DNA at (at least) two independent sites, one at the hinge and one at the globular domain that contains the SMC ATPase heads, the kleisin

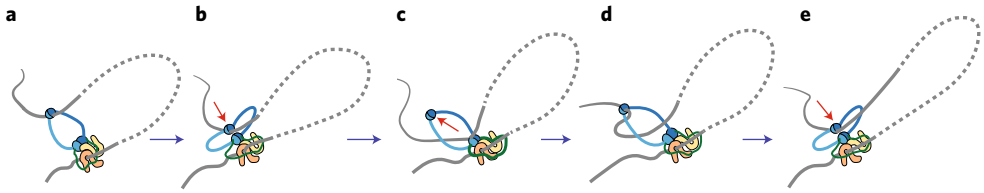

Fig. 6 | Scrunching model for condensin-mediated DNA loop extrusion. a–e, Condensin binds DNA tightly at the Ycg1–Brn1 anchor, as well as, transiently, to two other binding sites. From the open O shape (**a**), condensin collapses into the B shape (**b**) upon ATP binding, and the neck of the DNA loop concurrently changes from wide to narrow. Subsequently, the hinge is released (**c**), and the hinge reaches out to bind new DNA (**d**). Upon repeating this cycle, DNA is extruded into a loop (**e**).

subunit and the HEAT-repeat subunits. Previous work has clearly shown that Ycg1–Brn1 provides a strong DNA binding site[27], which is consistent with the observed DNA binding near the globular domain (Fig. 3a). The frequent occurrence of hinge binding that we observed is more surprising. Since the inner channel of the hinge domain has a positively charged surface, it is plausible that this might bind DNA[37]. Gel-shift assays and fluorescence anisotropy binding experiments indeed showed DNA binding affinity for the hinge domain of mouse condensin[37], yeast condensin[28] and bovine cohesin[38]. Previous AFM studies also showed DNA binding by the hinge domain of MukB[39] and of *S. pombe* condensin[21], suggesting a conserved hinge-binding mechanism. Our observation that the angle of coiled coils at the hinge of the O-shaped condensin can change dynamically (Extended Data Fig. 4a–c) furthermore indicates that the connection of the SMC arms to the hinge domain is flexible—consistent with a variety of angles observed previously in different crystal structures and a recent cryo-EM structure[37,40–43].

Implication for models of DNA-loop extrusion by SMC complexes. Given that it thus far has remained puzzling how the condensin complex is able to extrude a DNA loop, it is of interest to discuss what our findings imply for a mechanistic model for SMC-mediated DNA-loop extrusion. A working model should account for a number of specific experimental observations: it should (1) involve cyclic conformational transitions between an O shape and a B shape of the SMC complex, (2) be compatible with very flexible SMC arms, (3) accommodate a very large step size[14], (4) show a high correlation between the condensin size and the neck width at the stem of DNA loops (Fig. 5), (5) use the globular domain as a DNA anchoring site[14,27] and (6) use a DNA-binding site at the hinge domain.

Our experimental results do not support the 'tethered inchworm model' as proposed by Nichols and Corces[44] (Extended Data Fig. 10a), which predicts that DNA movement is driven by large changes in the distances between two DNA binding sites created by the two HEAT-repeat subunits when the conformation of the complex changes between V and I shapes. Our data showed that V- and I-shaped conformations were rare, and we observed a constant mutual distance between the Ycg1 and Ycs4 HEAT-repeat subunits over time. The 'DNA pumping model'[16] (Extended Data Fig. 10b) is also inconsistent with our observations. In this model, zipping-up of the SMC arms from an O into an I shape pushes DNA from the hinge to the head domains, whereupon a subsequent conformational change from an I to an O shape targets the capture of a new DNA segment. I shapes thus play a prominent role in the DNA pumping model. Yet, we only rarely observed I shapes in our images of the condensin holocomplex, both for the holocomplex on its own (Extended Data Fig. 4d–f) as well as for condensin bound to DNA (Fig. 3f). Instead, we observed conformational changes between O and B shapes, where B shapes do in fact not occur in the pumping model. Both these observations, the absence of I shapes and the prominence of B shapes, are in strong contrast to what would be expected for a DNA pumping model.

Our data instead indicate that some form of a 'scrunching model' underlies the motor action of SMCs (Fig. 6 and Extended Data Fig. 10c), where an SMC complex anchors to DNA and moves another piece of the DNA relative to this point to extrude a loop, by cyclically binding DNA at or close to the hinge and reeling it to the globular domain. In such a model, the hinge region binds DNA, transfers it to the head region, where it binds, upon which the hinge releases to subsequently grab a new piece of DNA to reel it in[13,45]. Our observation that condensin dynamically switches between an O shape and a collapsed B shape clearly hints at such a type of mechanism. Our finding that the hinge region binds DNA further supports this model. The flexible SMC arms provide a hint at the mechanism of DNA transfer from the hinge to the globular domain: while such flexible arms prevent a rigid-body power-stroke motion to directly transduce mechanical motion from the ATPase head domain to the (~37-nm) distant hinge domain, the arms instead may use thermal fluctuations to facilitate the motion of the DNA-bound hinge region to the globular domain as a biased-ratchet motor[46]. ATP binding may induce the interaction between the hinge and the head domains to form a B shape, whereas subsequent ATP hydrolysis may release the hinge (but not the DNA) from the globular domain to restart the cycle. During this cycle, the Ycg1–Brn1 anchor would ensure that condensin remains locked to DNA, such that the newly reeled-in DNA indeed translocates with respect to the anchor position, thus forming a DNA loop.

Such a scenario does imply the presence of another DNA-binding site (in addition to the hinge and the Ycg1–Brn1 anchoring site) in the globular domain that prevents slipping of the extruded DNA loop while the hinge is released in search of another piece of DNA. On the basis of previous suggestions for Rad50, prokaryotic SMC complexes and cohesin[26,47–50], it might be possible that such a third DNA-binding site is located in a positively charged cavity of the ATP-dimerized head domains or in the head-proximal coiled coils. With the new insights obtained in the present study, an important follow-up question is how unidirectionality of the loop-extrusion activity would be established in such a scrunching model. Perhaps the hinge domain is able to slide along the bound DNA double helix to ensure that it reels in DNA in the next cycle from the same side as in the previous reaction cycle, but this is merely a speculation and requires further research.

In conclusion, our experimental observations support a type of scrunching model in which a DNA-bound condensin extrudes a loop of DNA by cycling its conformation between O and B shapes. It will be of interest to also explore the motor mechanism for other SMC complexes, such as cohesin[26,29,51].

Online content

Any methods, additional references, Nature Research reporting summaries, source data, extended data, supplementary information, acknowledgements, peer review information; details of author contributions and competing interests; and statements of data and code availability are available at https://doi.org/10.1038/s41594-020-0508-3.

Received: 19 December 2019; Accepted: 20 August 2020;
Published online: 28 September 2020

References

1. Nasmyth, K. & Haering, C. H. The structure and function of SMC and kleisin complexes. *Annu. Rev. Biochem.* **74**, 595–648 (2005).
2. Haering, C. H. & Gruber, S. SnapShot: SMC protein complexes part I. *Cell* **164**, 326.e1 (2016).
3. Hirano, T. Condensin-based chromosome organization from bacteria to vertebrates. *Cell* **164**, 847–857 (2016).
4. Oliveira, R. A., Coelho, P. A. & Sunkel, C. E. The condensin I subunit Barren/CAP-H is essential for the structural integrity of centromeric heterochromatin during mitosis. *Mol. Cell. Biol.* **25**, 8971–8984 (2005).
5. Houlard, M. et al. Condensin confers the longitudinal rigidity of chromosomes. *Nat. Cell Biol.* **17**, 771–781 (2015).
6. Rao, S. S. P. et al. Cohesin loss eliminates all loop domains. *Cell* **171**, 305–320.e24 (2017).
7. Naumova, N. et al. Organization of the mitotic chromosome. *Science* **342**, 948–953 (2013).
8. Sanborn, A. L. et al. Chromatin extrusion explains key features of loop and domain formation in wild-type and engineered genomes. *Proc. Natl Acad. Sci. USA* **112**, E6456–E6465 (2015).
9. Fudenberg, G. et al. Formation of chromosomal domains by loop extrusion. *Cell Rep.* **15**, 2038–2049 (2016).
10. Dekker, J. & Mirny, L. The 3D genome as moderator of chromosomal communication. *Cell* **164**, 1110–1121 (2016).
11. Alipour, E. & Marko, J. F. Self-organization of domain structures by DNA-loop-extruding enzymes. *Nucleic Acids Res.* **40**, 11202–11212 (2012).
12. Goloborodko, A., Marko, J. F. & Mirny, L. A. Chromosome compaction by active loop extrusion. *Biophys. J.* **110**, 2162–2168 (2016).
13. Terakawa, T. et al. The condensin complex is a mechanochemical motor that translocates along DNA. *Science* **358**, 672–676 (2017).
14. Ganji, M. et al. Real-time imaging of DNA loop extrusion by condensin. *Science* **360**, 102–105 (2018).
15. Eeftens, J. & Dekker, C. Catching DNA with hoops—biophysical approaches to clarify the mechanism of SMC proteins. *Nat. Struct. Mol. Biol.* **24**, 1012–1020 (2017).
16. Diebold-Durand, M. L. et al. Structure of full-length SMC and rearrangements required for chromosome organization. *Mol. Cell* **67**, 334–347.e5 (2017).
17. Kamada, K., Su'etsugu, M., Takada, H., Miyata, M. & Hirano, T. Overall shapes of the SMC–ScpAB complex are determined by balance between constraint and relaxation of its structural parts. *Structure* **25**, 603–616.e4 (2017).
18. Soh, Y. M. et al. Molecular basis for SMC rod formation and its dissolution upon DNA binding. *Mol. Cell* **57**, 290–303 (2015).
19. Bürmann, F. et al. A folded conformation of MukBEF and cohesin. *Nat. Struct. Mol. Biol.* **26**, 227–236 (2019).
20. Lee, B. G. et al. Cryo-EM structures of holo condensin reveal a subunit flip-flop mechanism. *Nat. Struct. Mol. Biol.* https://doi.org/10.1038/s41594-020-0457-x (2020).
21. Yoshimura, S. H. et al. Condensin architecture and interaction with DNA. *Curr. Biol.* **12**, 508–513 (2002).
22. Eeftens, J. M. et al. Condensin Smc2-Smc4 dimers are flexible and dynamic. *Cell Rep.* **14**, 1813–1818 (2016).
23. Katan, A. J. & Dekker, C. High-speed AFM reveals the dynamics of single biomolecules at the nanometer scale. *Cell* **147**, 979–982 (2011).
24. Kodera, N., Yamamoto, D., Ishikawa, R. & Ando, T. Video imaging of walking myosin V by high-speed atomic force microscopy. *Nature* **468**, 72–76 (2010).
25. Uchihashi, T. et al. High-speed atomic force microscopy reveals rotary catalysis of rotorless F_1-ATPase. *Science* **333**, 755–758 (2011).
26. Shi, Z., Gao, H., Bai, X.-C. & Yu, H. Cryo-EM structure of the human cohesin-NIPBL-DNA complex. *Science* **368**, 1454–1459 (2020).
27. Kschonsak, M. et al. Structural basis for a safety-belt mechanism that anchors condensin to chromosomes. *Cell* **171**, 588–600 (2017).
28. Piazza, I. et al. Association of condensin with chromosomes depends on DNA binding by its HEAT-repeat subunits. *Nat. Struct. Mol. Biol.* **21**, 560–568 (2014).
29. Kim, Y., Shi, Z., Zhang, H., Finkelstein, I. J. & Yu, H. Human cohesin compacts DNA by loop extrusion. *Science* **366**, 1345–1349 (2019).
30. Japaridze, A. et al. Spatial confinement induces hairpins in nicked circular DNA. *Nucleic Acids Res.* **45**, 4905–4914 (2017).
31. Anderson, D. E., Trujillo, K. M., Sung, P. & Erickson, H. P. Structure of the Rad50·Mre11 DNA repair complex from *Saccharomyces cerevisiae* by electron microscopy. *J. Biol. Chem.* **276**, 37027–37033 (2001).
32. Moreno-Herrero, F. et al. Mesoscale conformational changes in the DNA-repair complex Rad50/Mre11/Nbs1 upon binding DNA. *Nature* **437**, 440–443 (2005).
33. Park, Y. B. et al. Eukaryotic Rad50 functions as a rod-shaped dimer. *Nat. Struct. Mol. Biol.* **24**, 248–257 (2017).
34. Lyumkis, D. Challenges and opportunities in cryo-EM single-particle analysis. *J. Biol. Chem.* **294**, 5181–5197 (2019).
35. Noble, A. J. et al. Reducing effects of particle adsorption to the air–water interface in cryo-EM. *Nat. Methods* **15**, 793–795 (2018).
36. D'Imprima, E. et al. Protein denaturation at the air-water interface and how to prevent it. *Elife* **8**, e42747 (2019).
37. Griese, J. J., Witte, G. & Hopfner, K. P. Structure and DNA binding activity of the mouse condensin hinge domain highlight common and diverse features of SMC proteins. *Nucleic Acids Res.* **38**, 3454–3465 (2010).
38. Chiu, A., Revenkova, E. & Jessberger, R. DNA interaction and dimerization of eukaryotic SMC hinge domains. *J. Biol. Chem.* **279**, 26233–26242 (2004).
39. Kumar, R. et al. The bacterial condensin MukB compacts DNA by sequestering supercoils and stabilizing topologically isolated loops. *J. Biol. Chem.* **292**, 16904–16920 (2017).
40. Haering, C. H., Löwe, J., Hochwagen, A. & Nasmyth, K. Molecular architecture of SMC proteins and the yeast cohesin complex. *Mol. Cell* **9**, 773–788 (2002).
41. Li, Y., Schoeffler, A. J., Berger, J. M. & Oakley, M. G. The crystal structure of the hinge domain of the *Escherichia coli* structural maintenance of chromosomes protein MukB. *J. Mol. Biol.* **395**, 11–19 (2010).
42. Niki, H. Open and closed questions about open and closed SMC. *Structure* **25**, 569–570 (2017).
43. Ku, B., Lim, J. H., Shin, H. C., Shin, S. Y. & Oh, B. H. Crystal structure of the MukB hinge domain with coiled-coil stretches and its functional implications. *Proteins Struct. Funct. Bioinforma.* **78**, 1483–1490 (2010).
44. Nichols, M. H. & Corces, V. G. A tethered-inchworm model of SMC DNA translocation. *Nat. Struct. Mol. Biol.* **25**, 906–910 (2018).
45. Hassler, M., Shaltiel, I. A. & Haering, C. H. Towards a unified model of SMC complex function. *Curr. Biol.* **28**, R1266–R1281 (2018).
46. Hwang, W. & Karplus, M. Structural basis for power stroke vs. Brownian ratchet mechanisms of motor proteins. *Proc. Natl Acad. Sci. USA* **116**, 19777–19785 (2019).
47. Liu, Y. et al. ATP-dependent DNA binding, unwinding, and resection by the Mre11/Rad50 complex. *EMBO J.* **35**, 743–758 (2016).
48. Seifert, F. U., Lammens, K., Stoehr, G., Kessler, B. & Hopfner, K. Structural mechanism of ATP -dependent DNA binding and DNA end bridging by eukaryotic Rad50. *EMBO J.* **35**, 759–772 (2016).
49. Woo, J. S. et al. Structural studies of a bacterial condensin complex reveal ATP-dependent disruption of intersubunit interactions. *Cell* **136**, 85–96 (2009).
50. Erickson, H. P. Size and shape of protein molecules at the nanometer level determined by sedimentation, gel filtration, and electron microscopy. *Biol. Proced. Online* **11**, 32–51 (2009).
51. Davidson, I. F. et al. DNA loop extrusion by human cohesin. *Science* **366**, 1338–1345 (2019).

Methods

Condensin holocomplex purification. We used the same protocol as previously reported[14] for the purification of *S. cerevisiae* condensin holocomplexes with all the subunits: wild-type complexes (Smc2–Smc4–Brn1–Ycs4–Ycg1), mutant complexes lacking Ycg1 (Smc2–Smc4–Brn1–Ycs4) and EQ mutant complexes ($Smc2_{E1113Q}$–$Smc4_{E1352Q}$–Brn1–Ycs4). Complexes were expressed from 2μ-based high-copy plasmids containing pGAL10-YCS4 pGAL1-YCG1 TRP1 and pGAL7-SMC4-StrepII$_3$ pGAL10-SMC2 pGAL1-BRN1-His$_{12}$-HA$_3$ URA$_3$. Cells were lysed in buffer A (50 mM TRIS-HCl pH 7.5, 200 mM NaCl, 5% (vol/vol) glycerol, 5 mM β-mercaptoethanol, 20 mM imidazole) supplemented with 1× complete EDTA-free protease inhibitor mix (11873580001, Roche) in a FreezerMill (Spex), cleared by centrifugation, loaded onto a 5-ml HisTrap column (GE Healthcare) and finally eluted with 220 mM imidazole in buffer A. Eluate fractions were supplemented with 1 mM EDTA, 0.2 mM PMSF and 0.01% Tween-20, incubated overnight with Strep-Tactin Superflow high-capacity resin (2-1208-010, IBA) and eluted with buffer B (50 mM TRIS-HCl pH 7.5, 200 mM NaCl, 5% (vol/vol) glycerol, 1 mM DTT) containing 10 mM desthiobiotin. After concentrating the eluate by ultrafiltration, final purification was proceeded by size-exclusion chromatography with a Superose 6 column (GE Healthcare) pre-equilibrated in buffer B containing 1 mM $MgCl_2$. Purified protein was snap-frozen and stored at −80 °C until use. Most of the time, however, fresh condensin that had not been frozen was used.

ATPase assay. We used a colorimetric phosphate-detection assay (Innova Biosciences) to measure the ATPase activity of condensin complexes. We mixed 50 nM condensin and 50 ng μl^{-1} λ-DNA (Promega) for 15 min in 40 mM TRIS-HCl pH 7.5, 50 mM NaCl, 2.5 mM $MgCl_2$, 2 mM DTT, 5 mM ATP. After 15 min of incubation at room temperature, the concentration of the released phosphate was measured following the manufacturer's protocol.

Sample preparation for dry AFM. For the condensin-only sample preparation, we deposited 5 nM condensin onto newly cleaved mica surface (or mice pretreated with 0.00001% polylysine in Extended Data Fig. 2) for various conditions, namely with/without ATP and for EQ mutant condensin holocomplex with ATP in B1 buffer (20 mM TRIS-HCl pH7.5, 50 mM NaCl, 2.5 mM DTT, and 2.5 mM $MgCl_2$). We used a 2.5-mM ATP concentration for WT + ATP or EQ + ATP conditions, and incubated the mixtures for 10 min. After depositing the sample for 20 s, we rinsed the mica using H_2O, and dried the sample by using a gentle stream of N_2. Then, we classified the structures into O, I or B shapes, or kleisin- or hinge-opened states.

For the study on DNA and condensin interactions, we mixed 3 ng μl^{-1} of λ-DNA (D1501, Promega) and 5 nM of condensin in an Eppendorf tube for a 10-min incubation to induce condensin-DNA interaction. We then added 1 mM ATP and incubated the sample for an additional minute. We deposited the samples onto 0.00001% (wt/vol) polylysine-treated mica for 20 s and rinsed the surface using 3 ml MilliQ water. Finally, we dried the sample using N_2 gas. For Extended Data Fig. 6, we incubated λ-DNA and 3 nM of EQ mutant with 2 mM ATP for 10 min, and then deposited the sample onto polylysine-treated mica, which was finally rinsed with 3 ml MilliQ water and the sample was dried.

To induce DNA-loop formation by condensin, we incubated 3 ng μl^{-1} of λ-DNA with 1.5 nM condensin for 5 min in B1 buffer, and added 100 μM of ATP to this solution. We then incubated the mixture for 4 min, an incubation time similar to the lag time between condensin arrival and the initiation of DNA compaction observed in a magnetic-tweezers experiment[53]. We then deposited the sample (volume of 7 μl) onto the polylysine-treated mica for 20 s, and rinsed the sample using 1 ml buffer containing 50 mM $MgCl_2$ to completely immobilize the DNA on the surface and to prevent DNA diffusion during the washing and drying steps. Then, the sample was rinsed with 1–3 ml MilliQ water. It was important to avoid stretching forces on the DNA during the drying process, since forces as low as ~10 pN are sufficient to disrupt the loops formed by condensin[22]. While rinsing the sample on the mica, we tilted the mica with a small angle (~10° with respect to horizontal direction) in order to reduce tension on the DNA sample, so that we could image condensins that localized to the bases of DNA loops. The sample was dried by a gentle stream of N_2. In the case of liquid-AFM imaging of the DNA loop with condensin (Fig. 4a), we immobilized the same DNA, condensin and ATP mixture on the mica surface with 0.3 mM spermidine. At high polylysine concentrations, DNA is strongly attached on the surface as soon as it deposited, which yields kinetic trapping[54]. The effective persistence length for such a projection is smaller than for an equilibrated structure that is obtained for DNA on $MgCl_2$-treated mica. To prevent a high density of kinetically trapped DNA loops, we minimized the polylysine concentration to 0.00001% (wt/vol), so that DNA was fixed onto the surface only intermittently using sparsely distributed polylysine molecules.

Dry AFM imaging. We performed our AFM measurements in air on a Bruker Multimode AFM, with a Nanoscope V controller and Nanoscope version 9.2 software. We used Bruker ScanAsyst-Air-HR cantilevers (nominal stiffness and tip radius 0.4 N m^{-1} and 2 nm, respectively) or Bruker Peakforce-HIRS-F-A (0.35 N m^{-1} and 1 nm). The imaging mode we used was PeakForce Tapping, with an 8-kHz oscillation frequency, and a peak force setpoint value less than 100 pN. For imaging the condensin structures, 3 μm × 3 μm scan areas with 2,048 × 2,048 pixels were recorded at 0.5-Hz scanning speed. To record condensin on DNA loops, images of 10 μm × 10 μm were imaged with 5,120 × 5,120 pixels at 0.2- to 0.7Hz scanning speed. All measurements were performed at room temperature.

Liquid AFM imaging. Freshly purified condensin holocomplex (2 nM, wild-type or EQ mutant with 2 mM ATP incubated for 5 min in an Eppendorf tube) that had not been frozen was deposited on freshly cleaved mica surface with an imaging buffer (20 mM TRIS-HCl pH 7.5, 50 mM NaCl, 2.5 mM $MgCl_2$, 1–2 mM ATP or without ATP, 2.5 mM DTT). After 10 s, the sample surface was rinsed with the imaging buffer. During the rinsing step, the sample was not dried. Following a published protocol[55], we imaged the sample with HS AFM (HS AFM 1.0, RIB) using Nanoworld SD-S-USC-f1.2-k0.15 (2-nm tip radius, $k = 0.15$ N m^{-1}, $f = 1.2$ MHz) or Nanoworld SD-S-USC-f1.5-k0.6 cantilevers (2-nm tip radius, $k = 0.6$ N m^{-1}, $f = 1.5$ MHz). Typically, a scan size of 100 nm × 100 nm and 100–150 scan lines were used, with 1- to 10-Hz frame rates. For minimizing and stabilizing the sample-tip interaction during imaging, we used a feedback mechanism on the second harmonic amplitude[52]. We reconstructed movie files and images using a Matlab script. Using a Matlab code, we measured the hinge-to-head distance of every frame by measuring the distance between the two centers of mass of hinge and head domains. The hinge angle was measured as the angle between the two SMC arms at the hinge domain. For the classification of the O shape and B shape in Fig. 2h, we counted O shapes and B shapes as those protein complexes for which the hinge-to-head distance was larger or smaller than 23 nm, that is, the value where the valley between the two Gaussian peaks was located in Fig. 2b.

Image processing. Before quantitative analysis, images were processed to remove background and transient noise data that would give false signals in automated analysis. This was done using Gwyddion version 2.53 (ref. [56]). To ensure that only the empty surface was used for background subtraction, an iterative procedure of masking particles and subtracting (planar and/or line-by-line) background polynomials was employed. Horizontal scars, which occur from time to time owing to feedback instabilities or particles sticking to the AFM tip, were selected and removed by Laplacian background substitution. Finally, we used the blind tip estimation and surface reconstruction algorithms in Gwyddion to reduce the effects of AFM tip convolution (the widening of features due to the finite size of the AFM tip) on our images. It has been shown that the tip shape can affect estimates of SMC protein volume[57]. Although blind tip estimation is not capable of fully correcting for the influence of tip shape, we found that it substantially improved the consistency of the volume estimates, and the increased contrast in the reconstructed images allowed for a better delineation of individual molecules in automated image quantification.

Characterizing the condensin complex from dry AFM images. The volume of condensin molecules was measured using a home-built Matlab code. Background noise was subtracted by the program, and both the area and mean height of the structure were measured with respect to the background surface. The volume was then calculated by multiplying the deduced area and height. The distributions of the volumes were confirmed by Gywddion. To measure the volume using Gywddion, a height mask was applied to cover the condensin, and grain measurement was used in order to determine the volume for the different masked objects.

Distances between the hinge and the globular domain were measured between the hinge and globular parts, using the line tool and measurement function of ImageJ. The hinge angle was determined by measuring the angle between two SMC arms at the hinge domain.

For the counting of DNA loops (Fig. 4c), we counted the number of loops per image area and we normalized that number by the entire DNA length that was contained within the image area. To obtain the fraction of loops with condensin at a stem (Fig. 4d), we normalized the number of loops where condensin localized at the stem of loops by the total number of loops with or without condensin at the stem. Note that loops without condensin at the stem can be formed during sample preparation because upon deposition of the long DNA molecule onto the mica surface, two DNA regions can randomly overlap to form an apparent loop-like structure on the surface. The occurrence of such loops in AFM images does not depend on condensin or ATP. By contrast, the number of loops that are extruded by condensin complexes critically depends on ATP hydrolysis.

Measurement of DNA length and DNA loop size. We wrote Matlab scripts that perform automated image analysis to deduce the path of the DNA in images. The following procedure was used to select pixels that belong to areas covered with DNA: the image was smoothed with a Gaussian filter ($\sigma = 0.5$ pixels, window size = 5 pixels), and pixels with a height of more than 0.15 nm were selected. To get rid of noise and contaminations, objects (contiguous selected areas) with a maximum height of <0.3 nm were removed from the selection, as were objects with an area of <1,000 nm^2. To selectively analyze DNA on the surface, we excluded DNA-unbound proteins on the background by excluding objects with boundary length-to-area ratio > 0.1 nm^{-1} and those with area-to-bounding-box-area ratio < 0.25. As there was virtually no difference in observed height between the

SMC arms and the DNA, condensin molecules touching the DNA were mostly included in the selection, and the total DNA-length estimate is therefore a slight overestimate. The objects selected in this way were identified to be DNA, and visual inspection confirmed that this was reliable. To subsequently obtain the DNA length, the objects were skeletonized, and the length was approximated as $d_p \times n_s$, with n_s the number of pixels of the skeleton, and d_p the linear size of a single image pixel. For measuring the size of individual loops, loops were identified manually and subsequently traced using DNA Trace software[58].

Estimation of the probability of accidental colocalization of condensin and DNA. The binding probability between condensin and DNA was estimated from AFM images as the fraction of proteins that overlapped with a DNA molecule. There is also a probability that a randomly deposited protein will overlap with DNA. This accidental colocalization probability is estimated as follows: we approximate the protein by its circumcircle with diameter D_p. To overlap with the DNA, the center of this circumcircle should be within a distance D_p / 2 from the DNA. With a random placement of a condensin complex to the surface, the probability of this occurring in colocalization with the DNA is equal to the relative area of the image occupied by the space between two curves parallel to the DNA with a distance D_p between them. If the total length of all DNA in the image is L_{DNA}, this area can be approximated by $D_p \times L_{DNA}$. See Extended Data Fig. 7a for a graphical illustration of this. Therefore, the probability of finding a randomly placed molecule colocalized with the DNA is:

$$P_{C,random} = \frac{L_{DNA} \times D_p}{A_i},$$

where A_i is the imaged area. We used a value of 40 nm for D_p, and with an average $L_{DNA} = 209$ μm DNA in a $10 \times 10\ \mu m^2$ image, the accidental colocalization probability is about 8%. Note that this is an overestimate, because the condensin complex is often elongated so that in many cases the circumcircle can touch the DNA but the protein does not, and furthermore the DNA is curved and as a result the area between the parallel curves is less than $D_p \times L_{DNA.}$

A similar line of reasoning can be applied to the localization of condensin at the loop stem (Extended Data Fig. 8c–e). Long DNA molecules that are attached to a surface have loops in them even in the absence of protein, simply owing to the deposition of the randomly coiled DNA to the surface. There is a small chance that a randomly deposited protein, that was not already bound to the DNA before, locates with a distance D_p from the loop crossing—a probability that can be calculated similarly to above. Furthermore, a condensin that was already bound to the DNA before it got deposited, can, by chance, get located at the loop crossing in the process of depositing the DNA to the surface. Combining these two terms leads to an expression for the probability that condensin is accidentally observed as colocalized with loop crossings, which equals the number of DNA-bound condensins that are randomly located at the stem of DNA loops divided by the total number of DNA-bound condensins:

$$P_{l,random} = \frac{2N_l D_p}{L_{DNA}} + \frac{\pi D_p^2 N_l N_p}{4 A_i N_b},$$

where N_l, N_p and N_b are the total number of loops, total number of proteins and the number of DNA-bound proteins in the image, respectively. For our typical conditions, this probability $P_{l,random}$ is estimated to be about 3.5%. See also Extended Data Fig. 8e.

Width distributions of DNA-loop neck and protein. The neck size of the DNA was measured using the height profile tool of ImageJ. We used the cross-section of the DNA region closest to the loop neck that did not overlap with the site of the protein. The DNA height profiles of the cross-section region showed two peaks, one from each side of the loop forming the neck, to each of which we fitted a Gaussian (Fig. 5a, bottom). The neck size was taken as the horizontal distance between the outer points of the full-width half maximums of these Gaussians. The distance was defined this way because it gives a consistent definition, both when the DNA molecules or parts of the condensin complex were or were not resolved as separate Gaussian peaks. The same procedure was followed for measurements of the width of the protein that was located at the neck site.

Loop extrusion visualization using single-molecule fluorescence microscopy. For the loop extrusion assay, we followed the protocol published by Ganji et al.[14].

Reporting Summary. Further information on research design is available in the Nature Research Reporting Summary linked to this article.

Data availability

Source data for Figs. 1d–g, 2b,c,e,g,h, 3f, 4c–e and 5a,b and an uncropped version of the gel shown in Extended Data Fig. 1a are available with the paper online. Original movies for Fig. 2, Fig. 4a and Extended Data Fig. 3a,b are provided as Supplementary Videos.

References

52. Schiener, J., Witt, S., Stark, M. & Guckenberger, R. Stabilized atomic force microscopy imaging in liquids using second harmonic of cantilever motion for setpoint control. *Rev. Sci. Instrum.* **75**, 2564–2568 (2004).
53. Eeftens, J. M. et al. Real-time detection of condensin-driven DNA compaction reveals a multistep binding mechanism. *EMBO J.* **36**, 3448–3457 (2017).
54. Rivetti, C., Guthold, M. & Bustamante, C. Scanning force microscopy of DNA deposited onto mica: equilibration versus kinetic trapping studied by statistical polymer chain analysis. *J. Mol. Biol.* **264**, 919–932 (1996).
55. Uchihashi, T., Kodera, N. & Ando, T. Guide to video recording of structure dynamics and dynamic processes of proteins by high-speed atomic force microscopy. *Nat. Protoc.* **7**, 1193–1206 (2012).
56. Nečas, D. & Klapetek, P. Gwyddion: an open-source software for SPM data analysis. *Cent. Eur. J. Phys.* **10**, 181–188 (2012).
57. Gwynn, E. J. et al. Using DNA as a fiducial marker to study SMC complex interactions with the atomic force microscope. *Biophys. J.* **102**, 839–848 (2012).
58. Japaridze, A. et al. Hyperplectonemes: a higher order compact and dynamic DNA self-organization. *Nano Lett.* **17**, 1938–1948 (2017).

Acknowledgements

We thank S. Bisht, J. Eeftens, M. Ganji, E. Kim, B. Pradhan, S. H. Rah, I. Shaltiel, J. van der Torre, and W. W. W. Yang for discussions. This work was supported by ERC grants SynDiv 669598 (to C.D.), Marie Skłodowska-Curie grant agreement No. 753002 (to J.-K.R.), CondStruct 681365 (to C.H.H.), the Netherlands Organization for Scientific Research (NWO/OCW) as part of the Frontiers of Nanoscience and Basyc programs and the European Molecular Biology Laboratory.

Author contributions

J.-K.R., C.D., A.J.K. and C.H.H. designed the experiments; J.-K.R., A.K. and T.W. performed the AFM experiments; E.V.D.S. and J.-K.R. purified condensin complex; J.-K.R., A.J.K. and T.W. contributed image analysis; J.-K.R. and R.D.G. performed the ATPase assay and single-molecule fluorescence assay; C.D. and C.H.H supervised the work; and J.-K.R., C.D. and A.J.K. wrote the manuscript.

Competing interests

The authors declare no competing interests.

Additional information

Extended data is available for this paper at https://doi.org/10.1038/s41594-020-0508-3.

Supplementary information is available for this paper at https://doi.org/10.1038/s41594-020-0508-3.

Correspondence and requests for materials should be addressed to C.D.

Peer review information Anke Sparmann was the primary editor on this article and managed its editorial process and peer review in collaboration with the rest of the editorial team.

Reprints and permissions information is available at www.nature.com/reprints.

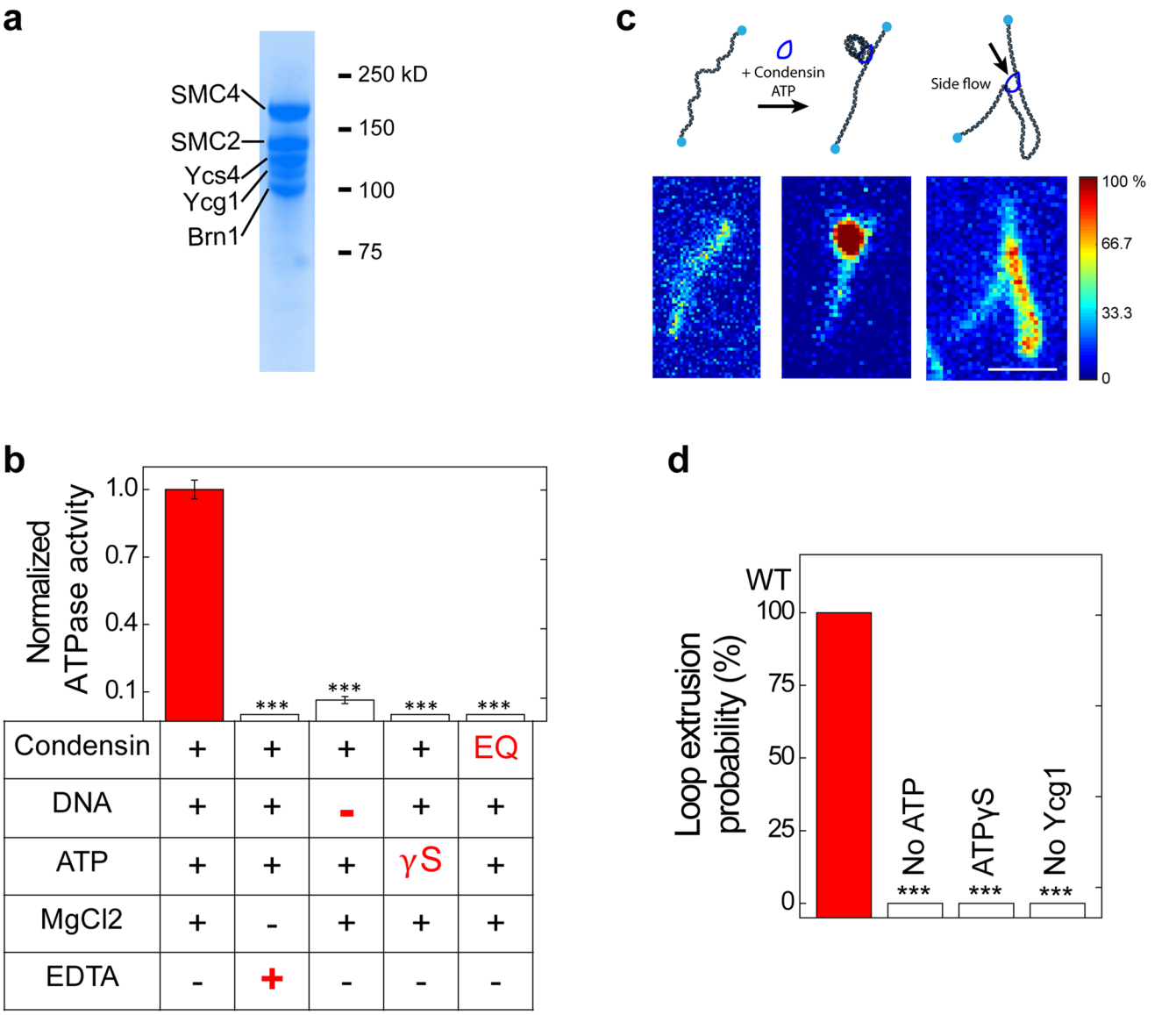

Extended Data Fig. 1 | Characterization of the functionality of yeast condensin. a, SDS page gel of the condensin proteins. **b**, ATPase activity of condensin with various controls ($N = 3$ independent experiments). Errors are s.d.. Uncropped image is available as source data. **c**, Loop extrusion assay with double tethered DNA showing that the condensin leads to the extrusion of a loop of DNA ($N = 3$ independent experiments and 200 molecules). **d**, Loop-extrusion probability with various negative controls ($N > 200$ molecules). In b and d, *** indicates $P<0.001$, assessed using two-tailed Student's *t*-test.

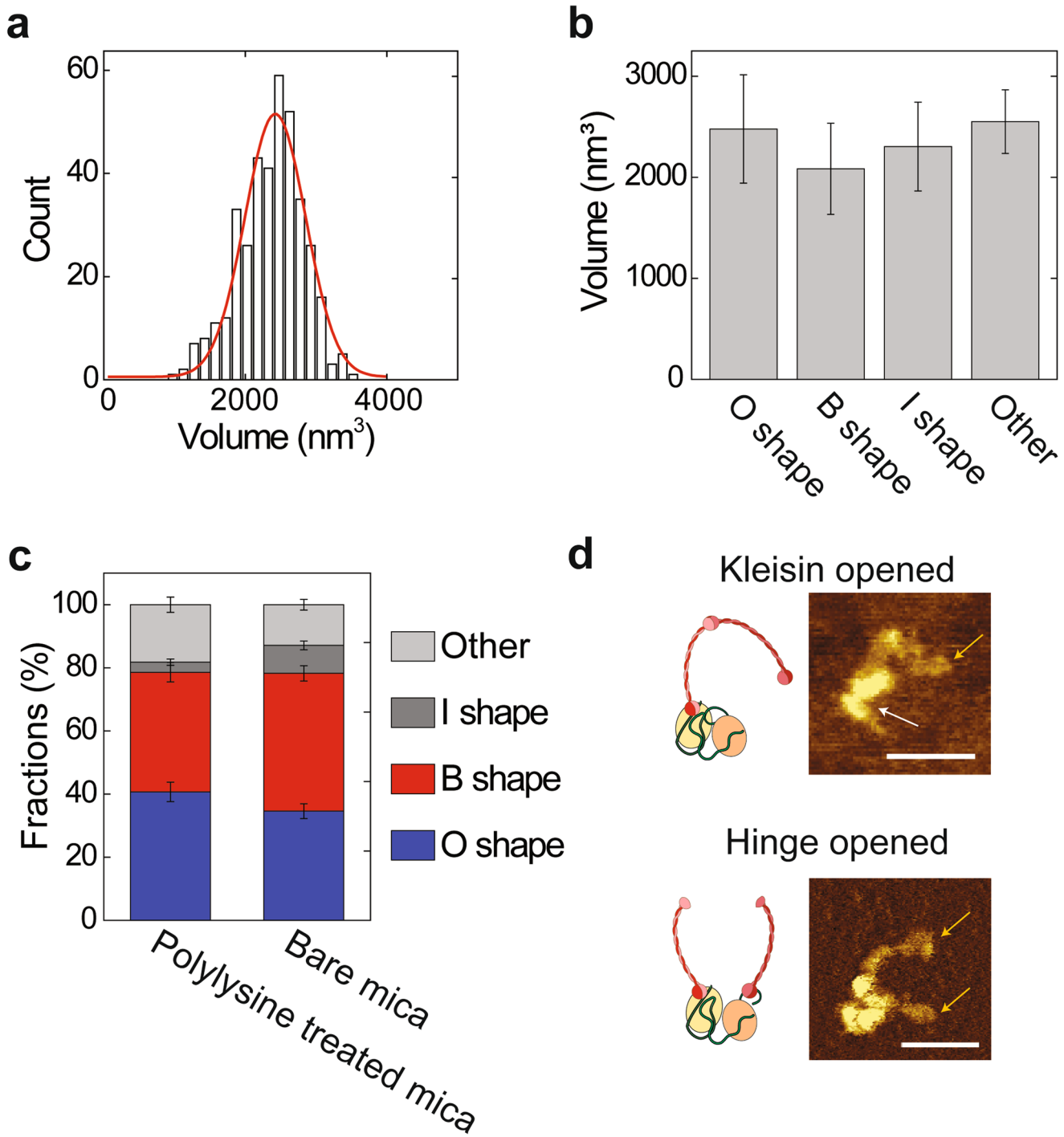

Extended Data Fig. 2 | Characterization of the condensin holocomplex. a, Frequency distribution of the condensin volume ($N = 3$ independent experiments and 384 molecules) as measured from dry AFM images. Gaussian fitting yielded a mean value of 2420 ± 430 nm³. **b**, Mean volume of each shape conformation ($N = 86$, 200, 51, and 47 for each state, respectively). Errors are s.d.. There were no significant differences in molecular volume between the states, consistent with the fact that each contained the same subunits. **c**, Relative occurrence of different shapes of condensin in AFM images taken in the presence of ATP on polylysine-treated mica ($N = 253$) versus images on bare mica ($N = 384$). Before sample deposition, polylysine was treated for 3 min, and the unbound polylysine was rinsed using distilled water. Errors are s.d. obtained by counting errors. **d**, Representative images that classified as other. Image of a 'kleisin-opened' state with a disconnection between one of the SMC heads and the non-SMC subunits (top) ($N = 21$ molecules). The white arrow indicates the non-SMC domains while the orange arrow points to an SMC end. AFM image of a 'hinge-opened' state where the two SMC arms were disengaged at the hinge ('hinge-opened shapes') ($N = 25$ molecules). The orange arrows indicate the dissociated hinge domains.

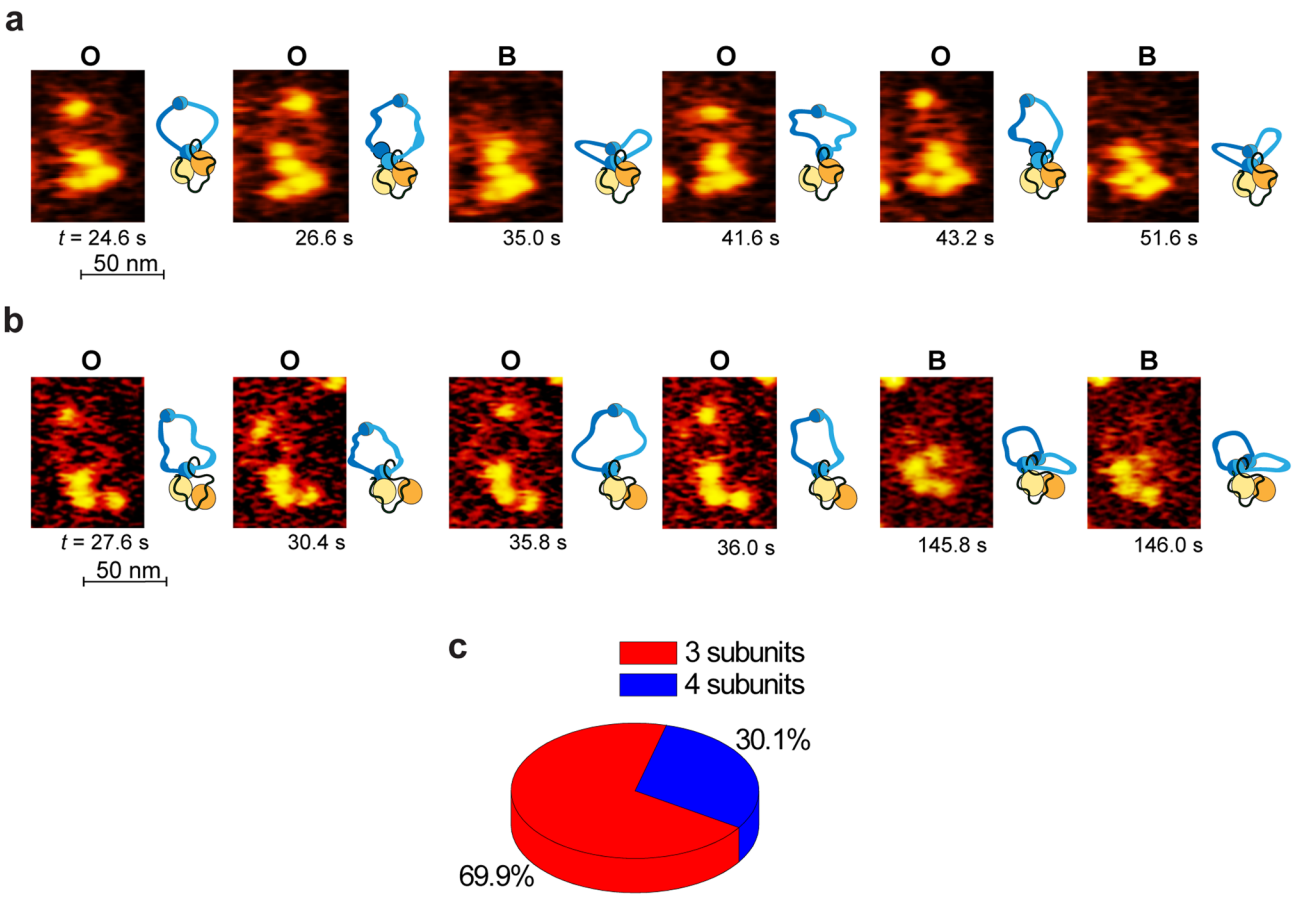

Extended Data Fig. 3 | Representative HS AFM image sequences of the condensin holocomplex in the presence of ATP. a, **b**, Images were taking from movies acquired at 5 frames/s rate, from Supplementary Video 2 in **a** and Supplementary Video 3 in **b (***N* = 6 molecules, 3 independent experiments, 2 independent protein purification, and 5,240 frames**)**. Changes between O- and B-shapes were observed. O and B indicate O-shape and B-shape, respectively. Cartoons on the right of each image are for visual guidance. **c**, Number of distinguishable subunits in the globular domain (that is, excluding the hinge) (*N* = 5,240 frames from 6 movies). About 70% of the complexes featured 3 distinguishable subunits in the globular domain, and about 30% featured 4 subunits. The complex with 3 subunits likely is composed of a dimerized head domain and two heat-domains, while two head domains were resolved separately in the case of the complex with 4 subunits in the globular domain.

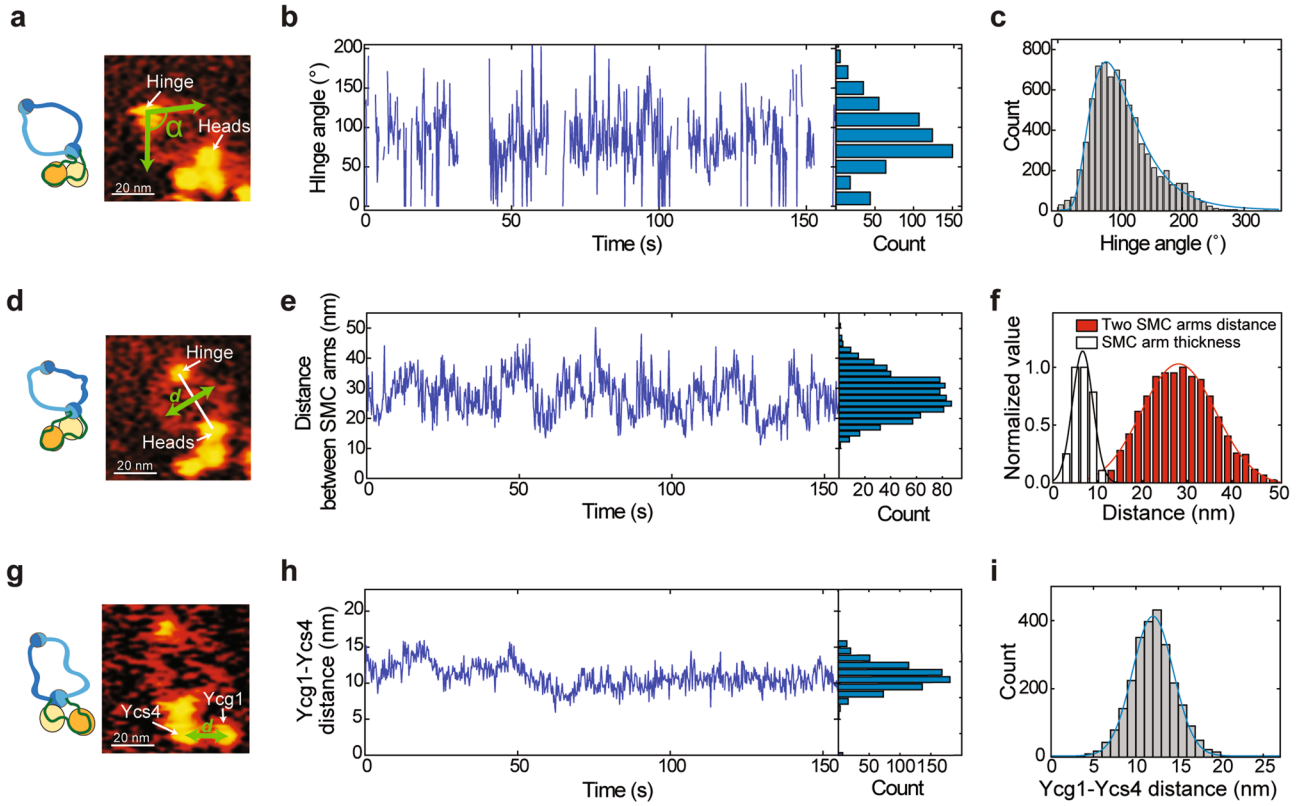

Extended Data Fig. 4 | Temporal fluctuations in the hinge angle, and distance changes between the two SMC arms and between the two HEAT domains. a, Snapshot image from a liquid AFM movie of a condensin holocomplex with the hinge angle indicated ($N = 3{,}780$ frames from 6 molecules). **b**, Representative trace of the hinge angle versus time. Right panel shows the distribution of the hinge angle from this trace ($N = 622$). **c**, Hinge angle distribution from 6 independent molecules ($N = 3{,}780$ frames). Fit is a lognormal distribution with a mean of 96° and a standard deviation of 48°, close to the hinge angle measured using dry AFM images (Fig. 1f). **d**, Snapshot image from a liquid AFM movie of a condensin holocomplex with the distance between two SMC arms indicated ($N = 2{,}315$ from 4 independent molecules). This mutual distance between the two SMC arms was measured along a line at the midpoint perpendicular (green) to a line (white) connecting the centers of mass at hinge and heads. **e**, Representative trace of the two SMC arms measured in a condensin holocomplex in the presence of ATP. Right panel shows the distribution of the distance between two SMC arms ($N = 789$). **f**, Distribution of the mutual distance between the two SMC arms obtained for 4 independent molecules ($N = 2{,}315$). Also plotted is the measured width for an individual SMC arm (FWHM of the cross-section of the arm) ($N = 88$). Fits are Gaussian distributions with 28.0 ± 8.1 nm and 6.6 ± 2.3 (mean ± s.d.) for the mutual distance and SMC arm thickness, respectively. **g**, Snapshot image from a liquid AFM movie with the Ycg1 and Ycs4 HEAT domains indicated for a condensin holocomplex where the two heads are dimerized ($N = 2{,}577$ from 4 independent molecules). **h**, Representative trace of the Ycg1-Ycs4 distance measured in a condensin holocomplex in the presence of ATP. Right panel shows the distribution of the Ycg1-Ycs4 distance from this trace ($N = 784$). **i**, The Ycg1-Ycs4 distance distributions obtained for 4 independent molecules ($N = 2{,}577$). Fit is Gaussian distribution with 12.0 ± 2.4 nm (mean ± s.d.).

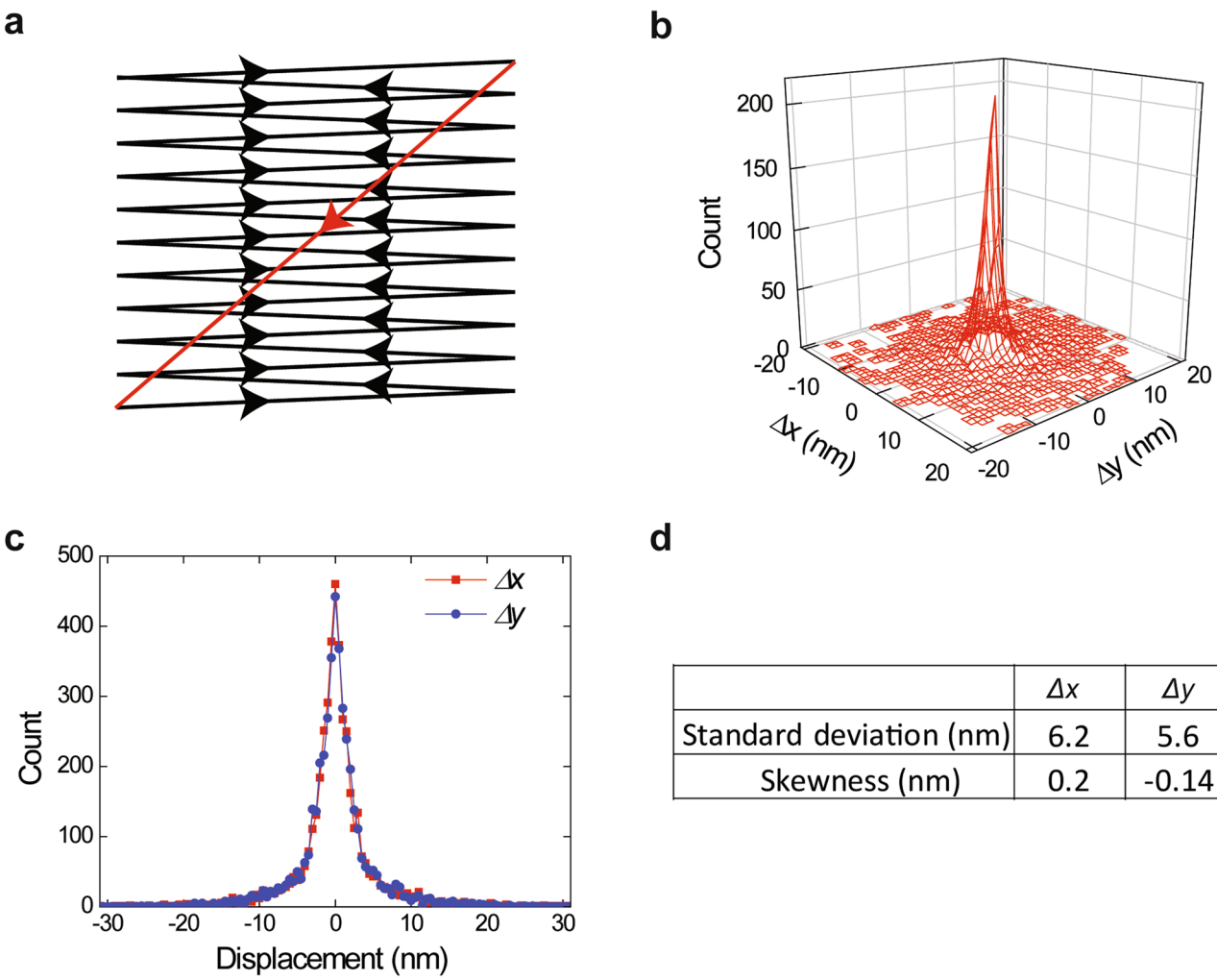

	Δx	Δy
Standard deviation (nm)	6.2	5.6
Skewness (nm)	0.2	-0.14

Extended Data Fig. 5 | Tip scanning direction does not bias the hinge motion. In HS AFM imaging in liquid, tapping and scanning the sample with the tip can potentially affect experiments adversely, for example induce a movement due to the tip pushing the molecule. The exact magnitude of the tip-sample forces in fluid tapping mode AFM is difficult to assess during imaging, but nevertheless can be qualitatively estimated from the magnitude of the second harmonic of the tapping signal[52]. We precisely controlled this and kept it to the minimum that still allowed for sufficient imaging resolution. To assess whether this was sufficient to avoid influencing the molecule dynamics, we analyzed the distribution of frame-to-frame position changes of the hinge domain with respect to the head domains. Since the scanning motion is not isotropic, one might expect an uneven distribution of hinge positional changes in the fast and slow scanning directions. Instead, we find a highly isotropic distribution, indicating minimal tip-induced effects. **a**, The zigzag scanning direction of HS AFM imaging. The horizontal direction scanning motion (black lines) is much faster than the vertical scanning. After finishing the imaging of a frame, the tip moves back to the starting point (red line) and scanning restarts. **b**, Surface plot of the two-dimensional histograms of the hinge domain displacement at all time points (N > 4,000 frames from 6 movies on different molecules). A radially symmetric distribution is obtained. No bias is observed towards a certain direction, also not towards the horizontal scanning direction (X-axis). **c**, The distributions of X, Y displacements between adjacent images are nearly identical. **d**, Tables of standard deviation and skewness of the X, Y displacements. Almost no skewness was observed in both cases.

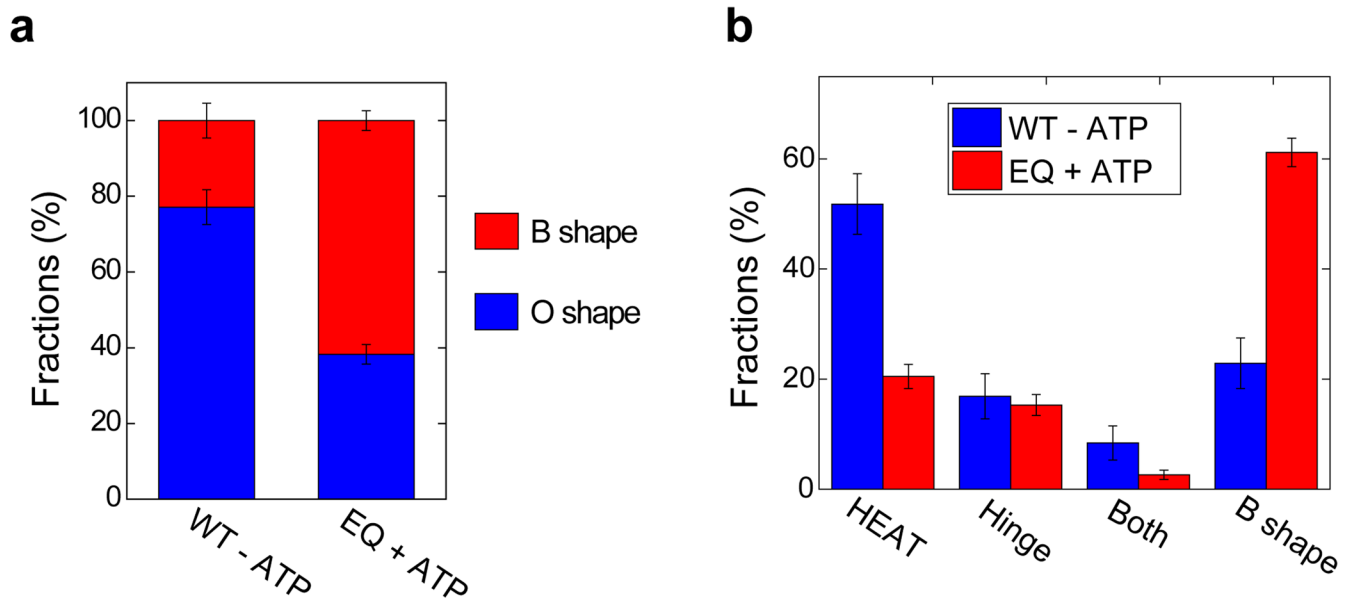

Extended Data Fig. 6 | Relative occurrence of different states of DNA-bound wild type condensin without ATP and EQ mutant plus ATP. a, Probability of the O-and B-shapes for condensin bound to DNA. **b**, Relative occurrence of each of the different binding modes. $N = 83$ and 347 molecules for wild type condensin without ATP and EQ mutant plus ATP, respectively. Errors are s.d. calculated by counting errors.

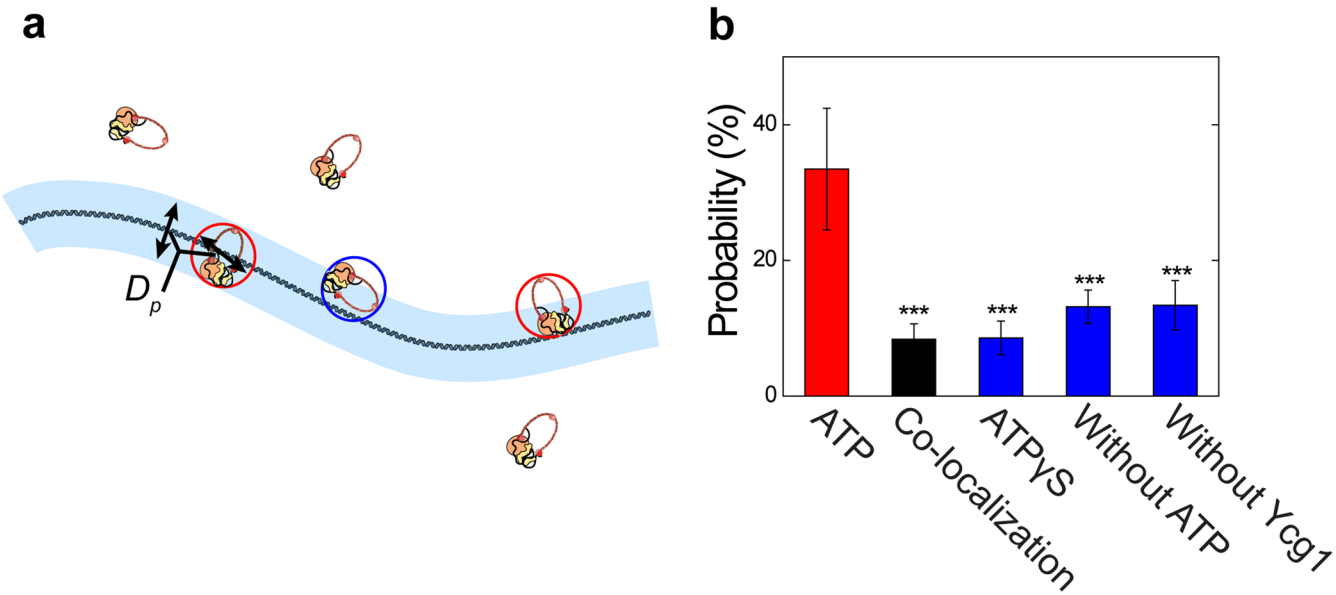

Extended Data Fig. 7 | Binding probability and co-localization probability of condensin on DNA. a, Schematic that illustrates the calculation of the probability for DNA and condensin to co-localize. Each condensin is approximated by a circumcircle with size D_p ~ 40 nm. The light blue shaded region indicates the area that should contain the center of the circumcircles for a randomly deposited condensin to co-localize with DNA. Condensin complexes inside the red circles overlap with DNA and would be counted as being bound in our measurements. Condensin complexes such as that in the blue circle are also included in the calculated co-localizing fraction, since their circumcircle overlaps with the DNA, even though the molecule itself does not touch the DNA. We deliberately err on the side of caution and do not correct for this, and the estimated value for the colocalization probability is therefore an upper bound. **b**, The DNA binding probability of condensin with ATP (red bar), the (inadvertent) colocalization probability of condensin (black bar), and DNA binding probability of condensin for negative controls (blue bars) The DNA binding probability of condensin is the observed binding probability, while the colocalization probability is the estimated probability that DNA and condensin accidently overlap on an AFM surface without biochemical interactions. N = 5, 5, 6, 8, and 5 independent experiments and errors are s.d., and *** indicates P<0.001, assessed using two-tailed Student's t-test.

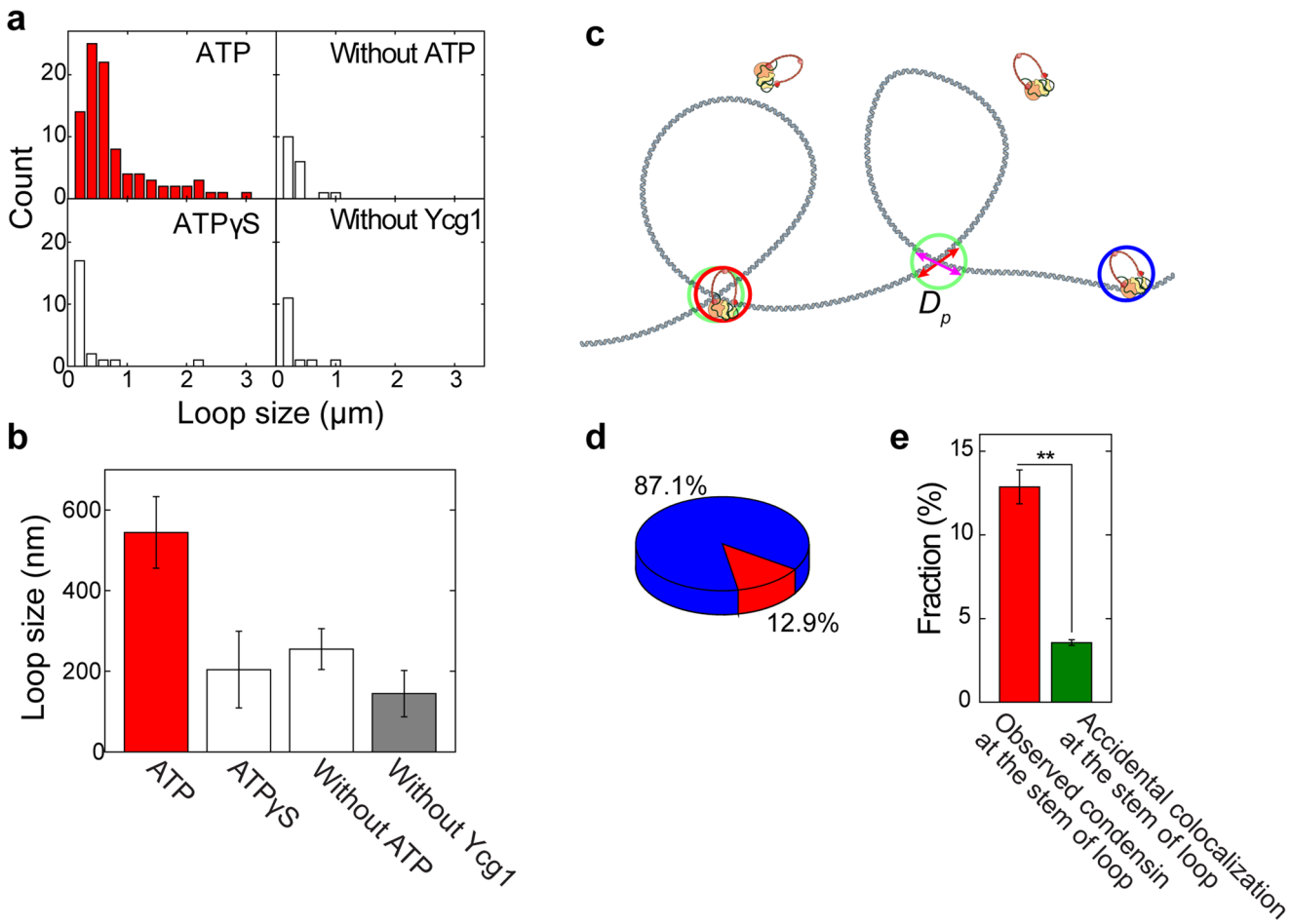

Extended Data Fig. 8 | Loop size and occurrence of condensin at the stem of DNA loops. a, DNA loop size distribution for data obtained with ATP, with ATPγS, without ATP, and without Ycg1 ($N = 94$, 22, 20, and 11 loops from 5, 6, 8, and 5 independent experiments, respectively). The importance of these data lies in the larger loop size observed with ATP as compared to the data in the other three controls. The actual value of the median loop size (0.54 μm in top panel) is in fact rather dependent on experimental conditions (for example incubation time) and limited by our finite imaging area (10 μm × 10 μm) and DNA overlap, which hampers clean identification of large loops in our experiments. Hence, we measured relative small loop sizes (< 1 μm) compared to earlier fluorescence microscopy experiments[14]. In the data presented here, we measured the size of loops where condensin localized at the stem. **b**, Loop size comparision in various conditions from a (median ± s.e.m.). **c**, Schematic to illustrate our estimate of the localization probability of condensin at the stem of the loop versus elsewhere on the DNA. Green circles denote the loop-stem area with a size D_p. Condensin occurring there (red circle) are counted 'at the loop stem', whereas all other DNA-bound condensin are counted 'not at the loop stem' (blue circle). **d**, Experimentally measured fractions of DNA-bound condensins that are observed at a loop stem (red), and not at a loop stem (blue) ($N = 5$ independent experiments). **e**, Fraction of DNA-bound condensins that are observed at a DNA loop stem (red), and the estimated accidental localization of condensin at a stem of DNA loops (green; $N = 5$ independent experiments) – see Material and Methods. Errors are s.e.m., and ** indicates $P<0.01$, assessed using two-tailed Student's t-test.

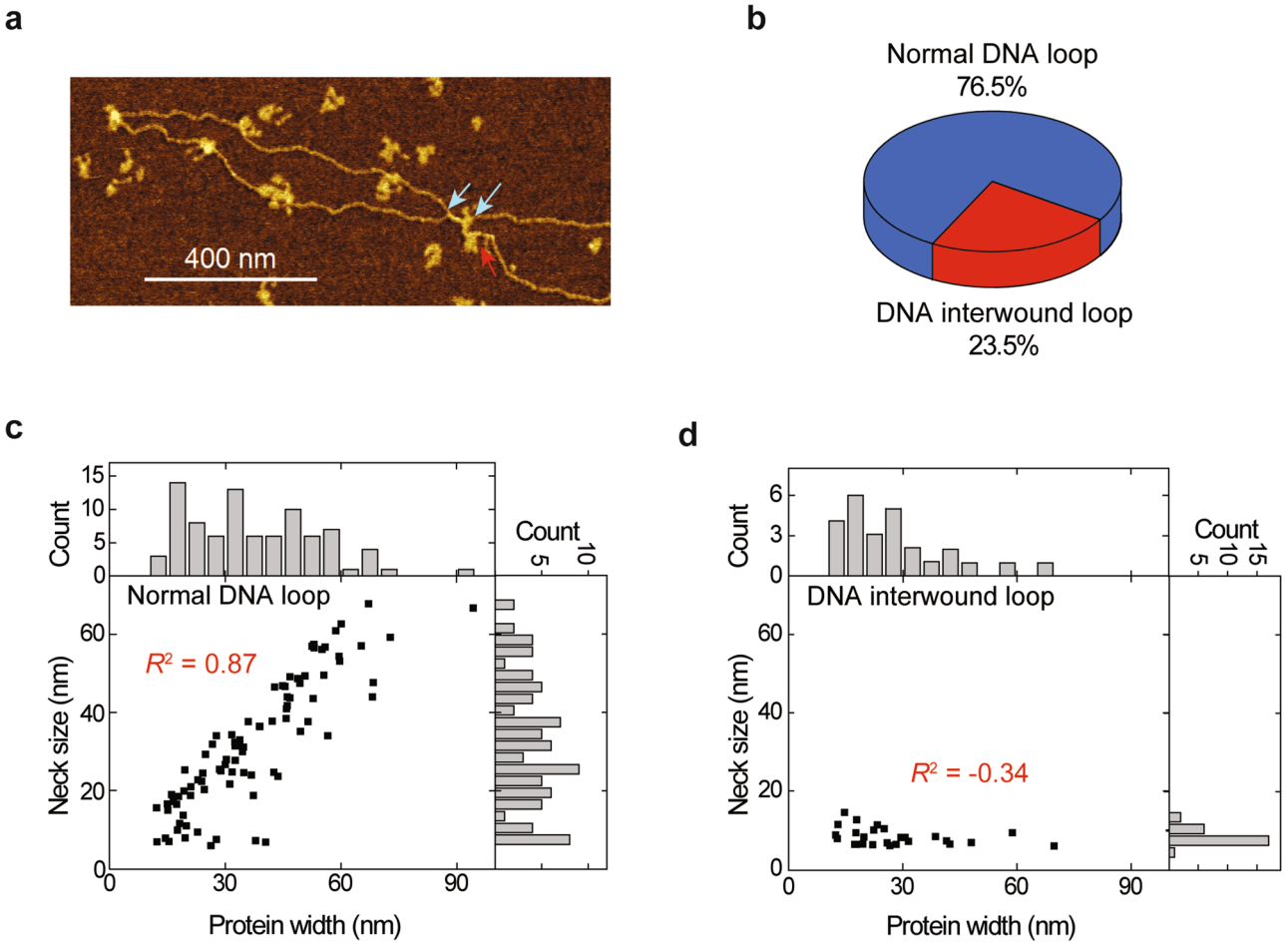

Extended Data Fig. 9 | Loops with an interwound DNA structure at the stem of loop. a, Example of an interwound DNA loop. Two arrows indicate the starting and ending points of an interwound DNA region. Yellow arrow indicates a condensin complex located near the loop stem. **b**, Fraction of loops with an interwound region at the stem ($N = 116$ molecules from 3 independent experiments). **c**, Scatter diagram of the protein width vs the neck size of normal (non-interwound) DNA loops ($N = 88$ loops). **d**, Idem for DNA interwound loops at the stem ($N = 27$ loops). A neck size of ~9 nm is observed, which may be attributed to the two parallel DNA molecules (that feature a ~2 + 2 nm dsDNA width), convoluted by the AFM tip size.

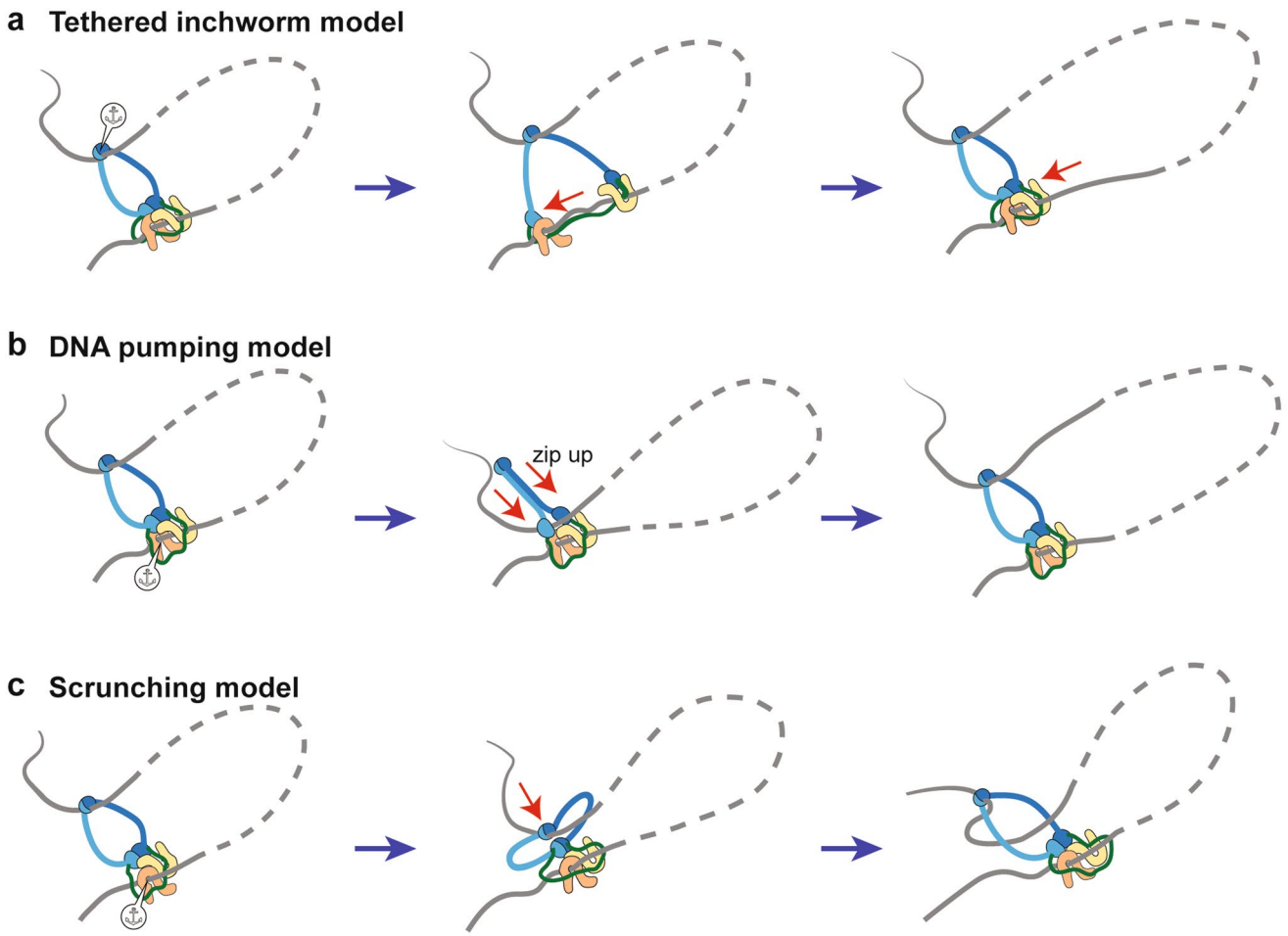

Extended Data Fig. 10 | Three different models of condensin-mediated DNA loop extrusion. a, Tethered inchworm model. Here, the hinge domain anchors the DNA. The two heads are tethered by Brn1 (green), which also binds Ycg1 and Ycs4, the HEAT subunits that bind DNA. In a cyclic fashion, associated with ATP hydrolysis, these two DNA-binding domains bind and unbind from DNA ('walk along the DNA') to pull in target DNA. **b**, DNA pumping model. Ycg1 (orange) anchors DNA while the hinge domain binds to another spot along the DNA. After ATP hydrolysis, the dissociation of dimerized head domains induces a conformational change of O shape to I shape of the SMC arms. Zippering of the SMC arms pushes the hinge-bound DNA region towards the head region. After ATP binding to the head domains, the hinge domain binds to new target DNA region, and the cycle is repeated for further DNA loop extrusion. **c**, Scrunching model. Ycg1 (orange) anchors DNA, and the hinge domain binds to a different spot along the DNA. Through conformational changes between O shape and B shape, the hinge transfers its bound DNA to the head domain, whereupon the hinge finds a new DNA target site for further DNA loop extrusion.

nature research

Corresponding author(s): Cees Dekker

Last updated by author(s): Aug 14, 2020

Reporting Summary

Nature Research wishes to improve the reproducibility of the work that we publish. This form provides structure for consistency and transparency in reporting. For further information on Nature Research policies, see our Editorial Policies and the Editorial Policy Checklist.

Statistics

For all statistical analyses, confirm that the following items are present in the figure legend, table legend, main text, or Methods section.

n/a	Confirmed	
☐	☒	The exact sample size (*n*) for each experimental group/condition, given as a discrete number and unit of measurement
☐	☒	A statement on whether measurements were taken from distinct samples or whether the same sample was measured repeatedly
☐	☒	The statistical test(s) used AND whether they are one- or two-sided *Only common tests should be described solely by name; describe more complex techniques in the Methods section.*
☐	☒	A description of all covariates tested
☒	☐	A description of any assumptions or corrections, such as tests of normality and adjustment for multiple comparisons
☐	☒	A full description of the statistical parameters including central tendency (e.g. means) or other basic estimates (e.g. regression coefficient) AND variation (e.g. standard deviation) or associated estimates of uncertainty (e.g. confidence intervals)
☐	☒	For null hypothesis testing, the test statistic (e.g. *F*, *t*, *r*) with confidence intervals, effect sizes, degrees of freedom and *P* value noted *Give P values as exact values whenever suitable.*
☒	☐	For Bayesian analysis, information on the choice of priors and Markov chain Monte Carlo settings
☒	☐	For hierarchical and complex designs, identification of the appropriate level for tests and full reporting of outcomes
☒	☐	Estimates of effect sizes (e.g. Cohen's *d*, Pearson's *r*), indicating how they were calculated

Our web collection on statistics for biologists contains articles on many of the points above.

Software and code

Policy information about availability of computer code

Data collection	The dry AFM images were collected via Nanoscope 9.2 while HS-AFM images were obtained using a custom Igor 7 software.
Data analysis	To measure the entire length of DNA in dry AFM images, a custom-written Matlab 2017b software was used. Sample characteristics were measured using Gwyddion 2.53. By using DNA trace software, the precise sizes of DNA loops were measured. ImageJ was used to measure protein widths and neck sizes of DNA loops.

For manuscripts utilizing custom algorithms or software that are central to the research but not yet described in published literature, software must be made available to editors and reviewers. We strongly encourage code deposition in a community repository (e.g. GitHub). See the Nature Research guidelines for submitting code & software for further information.

Data

Policy information about availability of data

All manuscripts must include a data availability statement. This statement should provide the following information, where applicable:

- Accession codes, unique identifiers, or web links for publicly available datasets
- A list of figures that have associated raw data
- A description of any restrictions on data availability

Source data for Fig. 1d–g, 2b, c, e, g, and h, 3f, 4c–e, and 5a, b are available with the paper online. Uncropped version of gel of Extended Data Fig. 1a is available with the paper online. Original movies for Fig. 2, Fig. 4a, and Extended Data Fig. 3 are provided by supplementary Videos.

Field-specific reporting

Please select the one below that is the best fit for your research. If you are not sure, read the appropriate sections before making your selection.

☒ Life sciences ☐ Behavioural & social sciences ☐ Ecological, evolutionary & environmental sciences

For a reference copy of the document with all sections, see nature.com/documents/nr-reporting-summary-flat.pdf

Life sciences study design

All studies must disclose on these points even when the disclosure is negative.

Sample size	Dry AFM images that show condensin's structure were obtained more than 7 times and they consistently produced similar results. In addition, we used more than 200 molecules to obtain statistics. For HS-AFM images, we performed 3 independent experiments and obtained 12 individual traces to study the conformational changes. The precise number of samples that support their respective findings are stated in the manuscript.
Data exclusions	We excluded data from AFM images of denatured proteins as they were not physiologically relevant structures.
Replication	All results in the paper are from the analysis of multiple experiments and all of the findings were reproducible. The specific number of replications are provided in the main text and figure legends.
Randomization	Every molecule in the image area was used for an analysis. All the samples used for the experiment, i.e. condensin, mica surface, buffer solutions, aliquots of fresh condensin from different preps, were randomized to ensure reproducibility.
Blinding	To classify condensin architecture for Fig. 1c-d, three different people confirmed the classification of the shapes of condensin structures. For Fig. 3, two people classified the binding status independently, and similar results were obtained as well.

Reporting for specific materials, systems and methods

We require information from authors about some types of materials, experimental systems and methods used in many studies. Here, indicate whether each material, system or method listed is relevant to your study. If you are not sure if a list item applies to your research, read the appropriate section before selecting a response.

Materials & experimental systems

n/a	Involved in the study
☒	☐ Antibodies
☒	☐ Eukaryotic cell lines
☒	☐ Palaeontology and archaeology
☒	☐ Animals and other organisms
☒	☐ Human research participants
☒	☐ Clinical data
☒	☐ Dual use research of concern

Methods

n/a	Involved in the study
☒	☐ ChIP-seq
☒	☐ Flow cytometry
☒	☐ MRI-based neuroimaging